Chapter 4: SYNTHESIS AND TRIBOLOGICAL BEHAVIOUR OF Ni ALLOY-BASED COMPOSITES CONTAINING Ag, Ag-rGO, AND Ag-(rGO-Ni)

This chapter begins with the results on the characterization of synthesized reduced graphene oxide (rGO), Ni-doped reduced graphene oxide (rGO-Ni), ball-milled powders, Ni alloy, and Ni alloy-based composites containing a combination of solid lubricants. The results on the microstructural characterization, friction, and wear behaviour of Ni alloy (N0), Ni alloy-10 wt.% Ag (NA), Ni alloy-10 wt.% Ag- 1.0 wt.% rGO (NAG), and Ni alloy-10 wt.% Ag-1.0 wt.% rGO-Ni (NANG) are also included in this chapter. An elaborate discussion on the observed friction and wear performance has been presented based on the features seen on the worn surfaces of Ni alloy-based composites and the counterface Si_3N_4 slid against them to develop an understanding of their tribological behaviour and to reveal the prevailing wear mechanisms.

4.1 RESULTS

4.1.1 Characterization of Materials

4.1.1.1 FTIR Spectra of GO, rGO, and rGO-Ni

Figure 4.1 depicts the FTIR spectra of GO, rGO, and rGO-Ni powders. The GO exhibits vibrational peaks at 3429, 1729, 1629, 1390, and 1101 cm^{-1}, revealing O-H stretch of hydroxyl groups, C=O stretch of carbonyl and carboxylic groups, overlapped features associated with C=C stretch of sp^2 carbon-based linkages and bending mode of trapped H_2O molecules, bending mode of O-H, and stretches of C-O-based functionalities [81]. These strong vibrational features have signified the abundance of oxygen-containing functional groups in the GO. The peaks corresponding to the C=O stretch have completely disappeared for rGO and rGO-Ni. In contrast, intensities of vibrational modes attributed to hydroxyl and C-O-based functionalities have notably decreased in the rGO and rGO-Ni samples. Furthermore, the intensification and shift of sp^2 carbon-based C=C stretch at 1567 cm^{-1} in FTIR spectra of rGO and rGO-Ni reveal the restoration of graphitic skeleton via chemical reduction of GO [82,83]. A weak vibrational peak at 666 cm^{-1}, attributed to Ni-O stretching, suggests the presence of NiO in rGO-Ni [84].

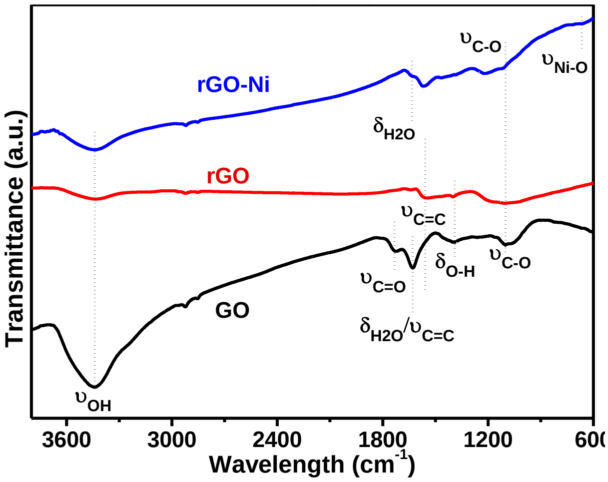

Fig. 4. 1 FTIR spectra of GO, rGO, and rGO-Ni, along with the assignment of vibrational peaks

4.1.1.2 XRD analysis of rGO and rGO-Ni

The crystalline features in rGO and rGO-Ni have been assessed by collecting their XRD patterns as shown in Figs. 4.2 (a and b). A diffraction peak at ~24.5° corresponding to the (002) plane with an interlamellar spacing of 0.36 nm has confirmed the restoration of van der Waals interactions-driven stacking of graphitic lamellae in the rGO (ICSD 98-005-2916) as seen from Fig. 4.2 (a). The intense diffraction features at 2θ ~44.4, 51.7, and 76.3° indicate the presence of the (111), (002), and (200) lattice planes of Ni (ICSD 076667), confirming the deposition of crystalline Ni nanoparticles over the rGO surface

[85]. The appearance of relatively weak and broad diffraction peaks at ~33.5 and 59.4° corresponding to the (101) and (110) planes of nickel hydroxides (ICSD 028101) have confirmed the formation of Ni $(OH)_2$ along with Ni [85,86]. An intense diffraction peak of nickel oxide (ICSD 076670) has been observed to coincide with the (111) plane of Ni; hence, the contribution of such phases is difficult to assess. However, a very poor diffraction peak at ~37.2° corresponding to the (111) plane of nickel oxide implies that the quantity of NiO is significantly low compared to nickel [86].

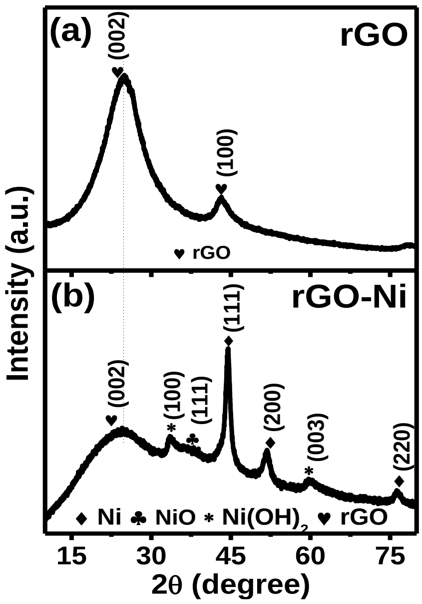

Fig. 4. 2 XRD patterns of (a) rGO and (b) rGO-Ni, along with the assignment of diffraction features

4.1.1.3 RAMAN analysis of rGO and rGO-Ni

The structural characteristics of graphene-based materials have been determined by non-destructive Raman spectroscopic measurements. The Raman spectra of rGO and rGO-Ni exhibit intense G and D bands in a spectral range of 1300 to 1600 cm^{-1}, as seen in Figs. 4.3 (a and b). The G band signifies sp^2-carbon based ordered hexagonal structure in the graphitic skeleton, whereas the D band represents disorderliness associated with sp^3 carbon, structural strain, edges, chemical functionalities, and structural flaws within a graphitic skeleton of rGO and rGO-Ni [87,88]. The G band for rGO and rGO-Ni has been found to occur at 1595 and 1588 cm^{-1}, respectively, whereas the D band of rGO and rGO-Ni has been observed to appear at 1339 and 1345 cm^{-1}, respectively. The shifting of the D band from 1339 cm^{-1} in rGO to 1345 cm^{-1} in rGO-Ni may be attributed to the loss of long-range periodicity due to the deposition of Ni nanoparticles on the graphitic skeleton [89]. The second-order phonon modes of the graphitic structure have been observed in a spectral range of 2500 to 3300 cm^{-1}. These modes at 2700, 2931, and 3193 cm^{-1} signify the 2D, D+G, and 2G overtone bands in rGO and rGO-Ni [90].

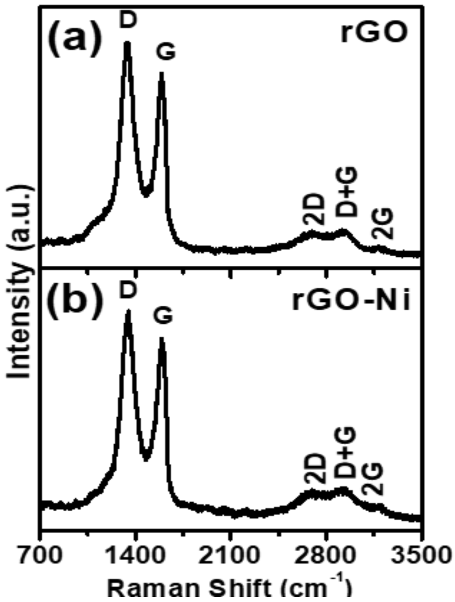

Fig. 4. 3 Raman spectra of (a) rGO and (b) rGO-Ni, along with assignment of Raman active modes

4.1.1.4 TEM analysis of rGO and rGO-Ni

The microstructural features of rGO and rGO-Ni, along with the distribution of Ni nanoparticles on the surface of rGO sheets, have been probed by capturing their HRTEM images. The rGO exhibits sheets-like structures with many folds and wrinkles as seen from

Figs. 4.4 (a-c). The TEM image of rGO-Ni shows crumpled rGO sheets along with deposition of Ni nanoparticles throughout their surfaces as seen from Figs. 4.4 (d-e). The size of these nanoparticles is found to vary from 3-15 nm. The graphitic lamellae are explicitly seen in high-resolution images of rGO-Ni as shown in Figs. 4.4 (g-h). As indicated by white arrows in high-resolution micrographs (Figs. 4.4 (f, h, and i)), the Ni nanoparticles with different crystalline fringes and irregular spherical shapes are observed on the edges and surface of rGO lamellae in the rGO-Ni. The elemental mapping of the rGO-Ni displays regularly distributed pixels associated with C, O, and Ni as illustrated in Fig. 4.4 (j). The intense and regular distribution of C and O signify the rGO, whereas the uniformly distributed comparatively lesser intensity of Ni reveals the regular deposition of Ni nanoparticles in the rGO-Ni, which is further supported by electron micrographs as illustrated in Figs. 4.4 (d-e).

4.1.1.5 XPS analysis of rGO and rGO-Ni

The C 1s spectra of rGO and rGO-Ni exhibit a broadened peak with an intense shoulder at higher binding energy, as seen in Figs. 4.5 (a and d). A most important peak component at 284.5 eV pertaining to C=C represents the sp^2 carbon-based network of graphitic structure in both rGO and rGO-Ni. The deconvoluted peak components at 286.2 and 288.2 eV with low peak intensities signify C-O and COOH-based residual functionalities in both rGO and rGO-Ni. A peak at 290.6 eV corresponding to the π-π^* transition suggests the presence of the delocalized conjugation in the graphitic network [91]. The O1s spectrum of rGO (Fig. 4.5 (b)) has been deconvoluted into chemically shifted three peaks at 531.1, 532.2, and 533.3 eV, corroborating O-H, C-O, and C=O functionalities. The O1s spectrum of rGO-Ni exhibits an additional peak at 530.7 eV, signifying the Ni-O linkages.

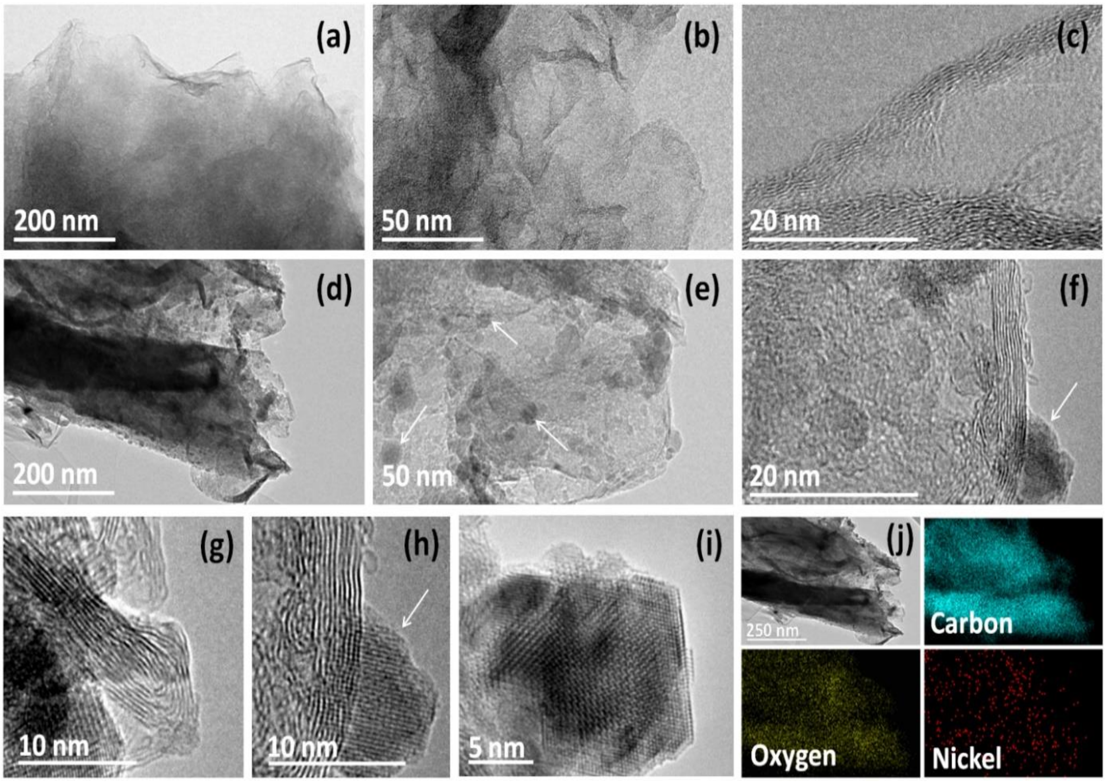

Fig. 4. 4 TEM images of (a-c) rGO and (d-i) rGO-Ni at different magnifications. In high-resolution images (g-h) graphitic lamellae, and (e-f, h-i) Ni-based nanoparticles are explicitly seen in rGO-Ni. (j) Electron micrograph along with corresponding are a elemental mapping (C, O, and Ni) of rGO-Ni

The high-resolution Ni 2p spectrum of rGO-Ni has exhibited two primary peaks at 855.5 and 873.0 eV, representing Ni $2p_{3/2}$ and Ni $2p_{1/2}$, respectively, as seen from Fig. 4.5 (f). The doublet of Ni 2p contains broad satellite peaks at 861.2 and 879.2 eV with a spin-orbital difference of 18.0 eV. The presence of mixed valence states [Ni (0) and Ni (II)] in the material has also been confirmed by Ni $2p_{3/2}$ and Ni $2p_{1/2}$ deconvoluted peak components. The existence of doublet peaks at higher binding energies (855.2 and 856.4 eV) implies the oxygenated form of nickel, i.e., NiO and Ni $(OH)_2$. The doublet at lower binding energy (852.6 eV) has revealed Ni (0) form. The XPS, a highly surface-sensitive tool within the 2-3 nm analysis range, encompasses surface functionalities of Ni-based particles. Hence, it has shown a higher intensity of oxygen-based Ni (II) functionalities [92,93].

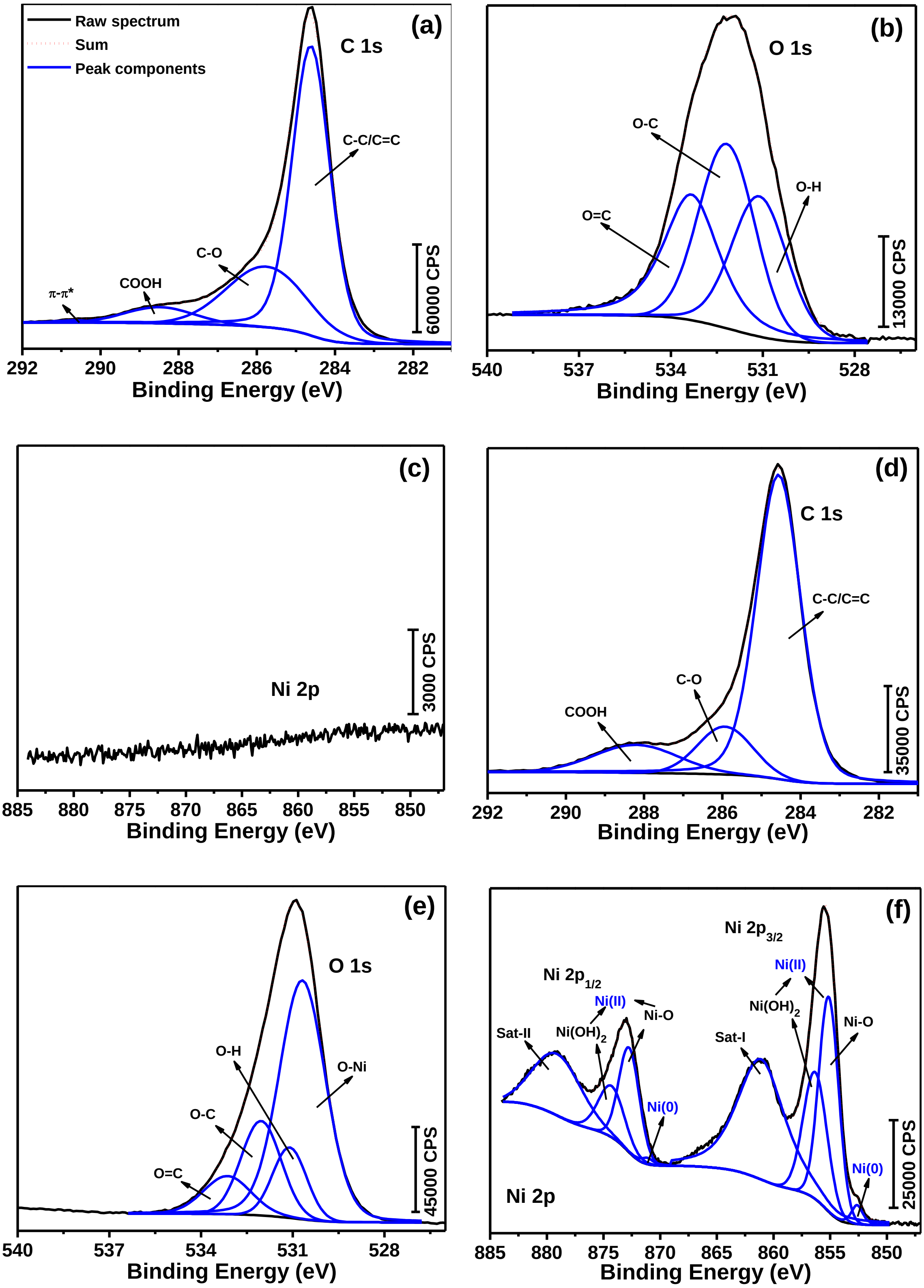

Fig. 4. 5 High-resolution (a) C 1s, (b) O 1s, and (c) Ni 2p XP spectra along with deconvoluted peak components of rGO. (d) C 1s, (e) O 1s, and (f) Ni 2p XP spectra along with deconvoluted peak components of rGO-Ni

4.1.1.6 Morphology of ball-milled powders and composites

Figure 4.6 presents the morphology of the initial powders as examined under SEM. The particles of Ni and Mo powders (Figs. 4.6 (a and c)) appear to be spherical whereas those of Cr and Ti (Figs. 4.6 (b and d)) are angular in shape with sharp/rounded edges, respectively. The powder of Al reveals a mixture of spherical and rounded shapes as shown in Fig. 4.6 (e). However, the particles of Ag powder have irregular shapes, and that of Ni-doped rGO have a flaky appearance as seen from Fig. 4.6 (f). X-ray diffraction analysis (Fig. 4.6 (g) has shown the presence of Ni, Cr, Mo, Ti, Al, and Ag powders.

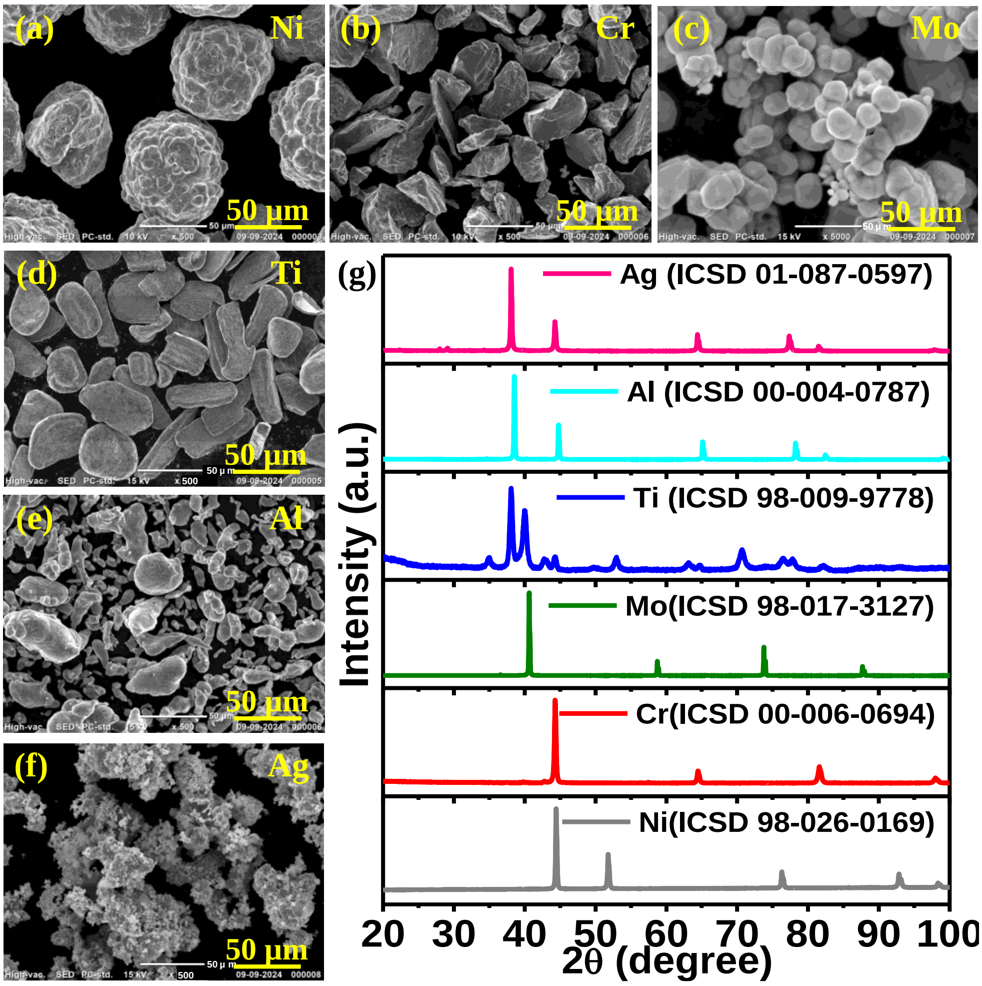

Fig. 4. 6 SEM image of elemental powders (a) Ni, (b) Cr, (c) Mo, (d) Ti, (e) Al, and (f) Ag, along with (g) their XRD pattern

A significant change in the morphology of the milled powders can be seen in Fig. 4.7. The fragmentation of flattened particles can be seen in milled powders for all powders. The average size of particles of the base alloy increases from 51.5 to 54.4 µm with addition of Ag alone as shown in Figs. 4.7 (a and b). The addition of the combinations of Ag-rGO and Ag-rGO-Ni in the base alloy leads to the reduction in the average size of the particles from 51.5 to 50.8 to 41.6 µm as seen from Figs. 4.7 (a-d).

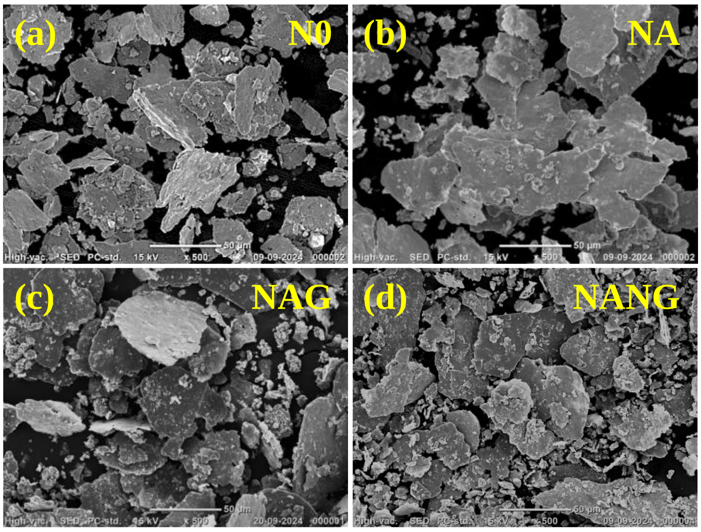

Fig. 4. 7 FESEM images of milled powders (a) N0, (b) NA, (c) NAG, and (d) NANG

The XRD patterns shown in Figs. 4.8 (a and b) reveal the crystalline features of milled powders and sintered composites, respectively. The diffraction peaks at ~ 44.40 and 76.31° corresponding to the (111), and (022) planes of Ni (ICSD 98-026-0169 could be observed in Fig. 4.8 (a) apart from peaks pertaining to Cr and Mo. The diffraction peaks at 2θ of ~51.76, 64.79, 81.68, and 93.10° correspond to (002), (200), (211), and (220) planes of Cr (ICSD 00-006-0694). Peaks at 2θ of ~40.57, 58.69, and 73.54° are attributed to the (011), (002), and (112) planes of Mo (ICSD 98-017-3127). One may also observe the additional peaks corresponding to Ag at ~38.15 and 81.64°, which have been attributed to the (111) and (222) planes of the Ag in the powder mixtures of NA, NAG, and NANG.

However, the peaks corresponding to rGO could not be observed in the powder mixture of NAG and NANG, probably due to its amount being below the detection limit of the instrument.

The XRD pattern of sintered base alloy (N0) presented in Fig. 4.8 (b) shows the peaks at ~ 42.04, 45.34, and 76.95° corresponding to the (111), (012), and (022) planes of Ni and diffraction peaks belonging to (002), (200), and (220) planes of Cr at 2θ of ~ 49.66, 63.55, and 91.03°. The peak at 2θ of ~74.23° corresponds to the (122) plane of Mo, whereas the peak at ~36.89° pertains to the (002) plane of Ti. The additional peaks at ~36.88 and 80.76° corresponding to (111) and (222) planes of Ag could also be seen in XRD patterns of NA, NAG, and NANG. However, no peaks corresponding to rGO could be observed in the diffraction patterns of sintered NAG and NANG for the reason mentioned earlier. An additional peak corresponding to the (011) plane of MoC (ICSD 98-007-7157) has been observed at ~37.18° in NAG and NANG. MoC may have formed within the composite during spark plasma sintering through interactions between Mo and rGO [55]. X-ray diffraction patterns of the sintered N0, NA, NAG, and NANG affirm that no oxidation has taken place during the sintering of the powders under vacuum conditions.

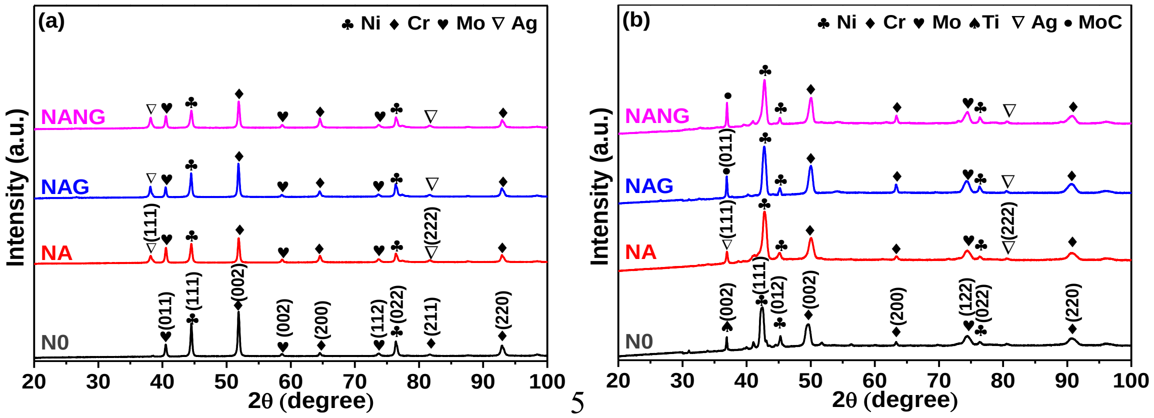

Fig. 4. 8 X-ray diffraction patterns of (a) ball milled powder and (b) spark plasma sintered composite for N0, NA, NAG, and NANG

FESEM micrographs of the sintered N0, NA, NAG, and NANG have been presented in Figs. 4.9 (a-d), along with their area elemental distribution. The microstructure of N0 reveals the existence of a Ni alloy-based solid solution as shown in Fig. 4.9 (a), the light grey areas show the presence of Ag in the Ni alloy-based matrix as shown in Fig. 4.9 (b). The black and light grey regions in the microstructure of NAG and NANG reveal the existence of rGO and Ag, respectively, in the matrix as seen from Figs. 4.9 (c and d)). However, one may observe the size of grey and black regions is relatively fine in the microstructure of NANG compared to NAG as seen from Figs. 4.9 (c and d)), which suggests a lesser possibility of agglomeration and a uniform distribution of constituent elements. The EDS analysis of the regions marked as 1, 2, and 3 in the microstructure of NANG (Fig. 4.9 (d)) reveals that region 1 (light grey area) is Ag rich, region 2 (black area) is C rich, representing rGO, and region 3 (grey area) is Ni alloy-based solid solution as seen from EDS patterns given in Fig. 4.10.

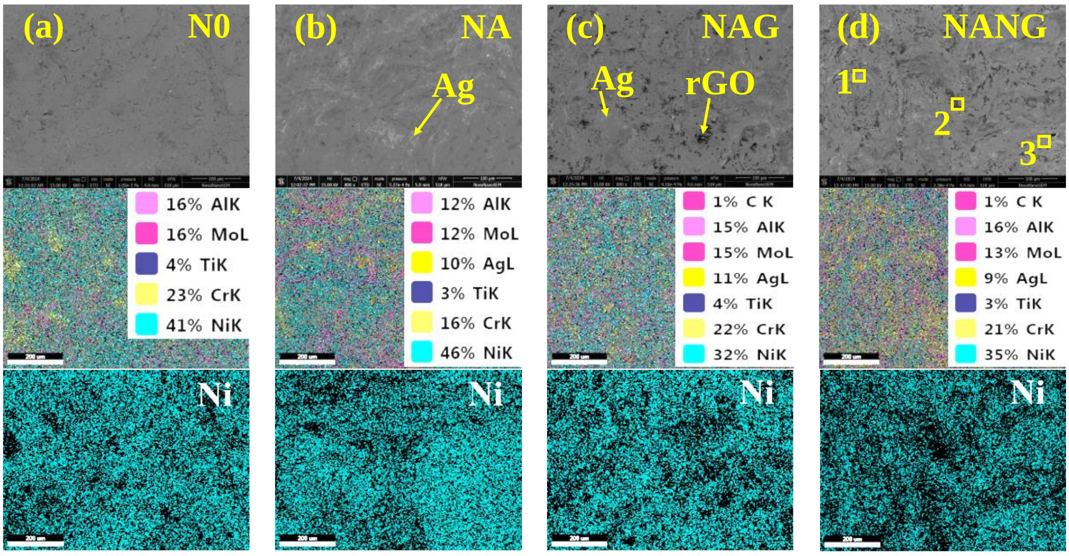

Fig. 4. 9 FESEM micrographs of (a) N0, (b) NA, (c) NAG, and (d) NANG along with their corresponding area elemental distribution (Ni, Cr, Mo, Ti, Al, Ag, C) and wt.% of each element

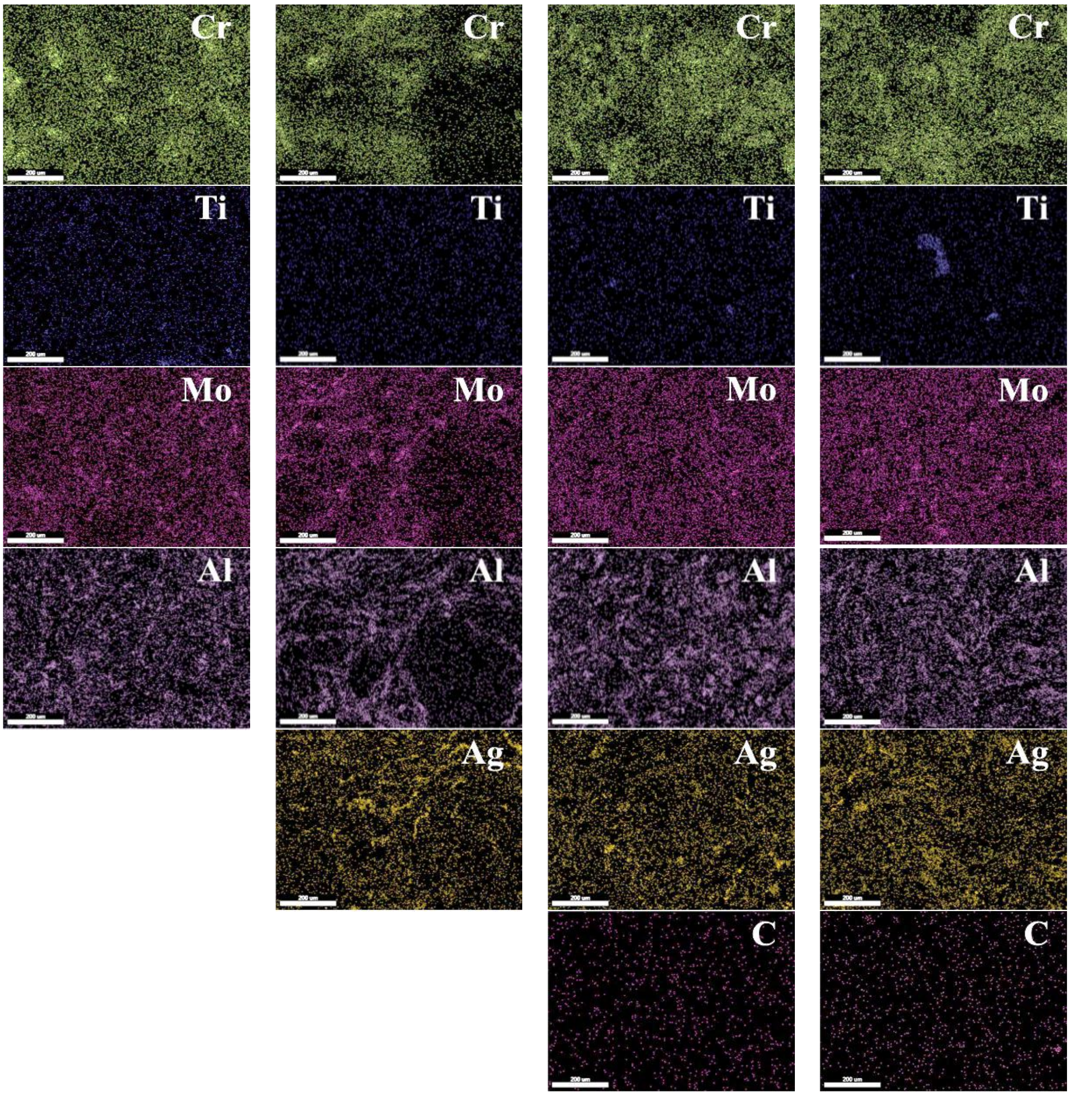

Fig. 4.9 Contd.

4.1.1.7 Hardness and density measurements

The designation, composition, density, and micro-hardness of all the sintered specimens are given in Table 4.1. The hardness of N0 is estimated as 515 ± 5 $HV_{0.3}$, and it reduces to 497 ± 4, 503 ± 6, and 510 ± 3 $HV_{0.3}$ with the incorporation of 10 wt.% Ag for NA, 1 wt.% rGO along with 10 wt.% Ag for NAG, 1 wt.% rGO-Ni, and 10 wt.% Ag for NANG, respectively.

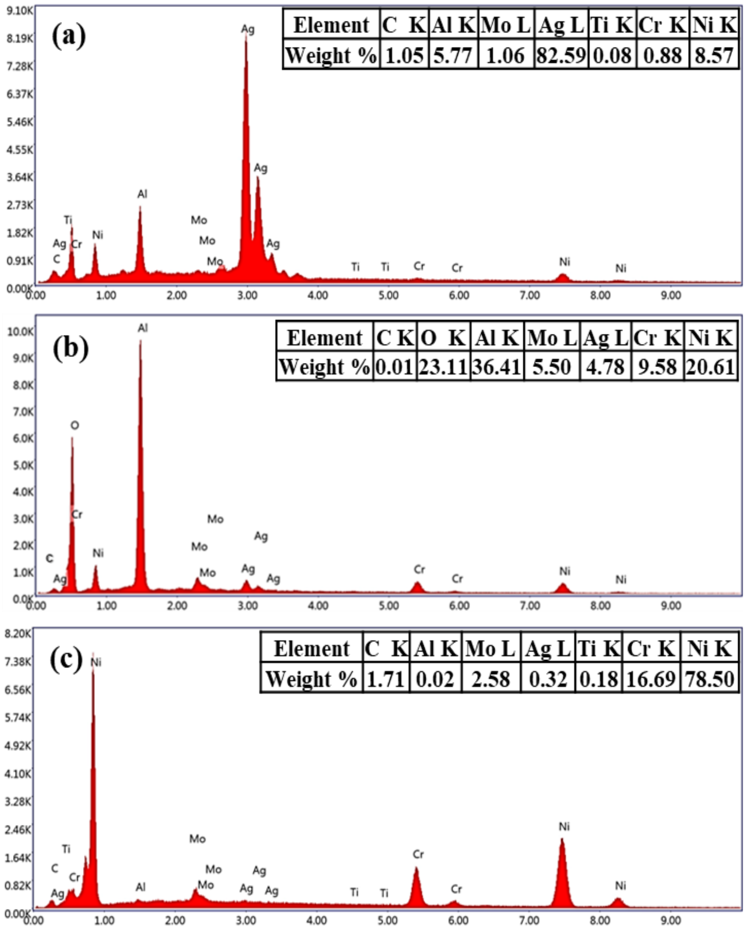

(a)

Element	C K	Al K	Mo L	Ag L	Ti K	Cr K	Ni K
Weight %	1.05	5.77	1.06	82.59	0.08	0.88	8.57

(b)

Element	C K	O K	Al K	Mo L	Ag L	Cr K	Ni K
Weight %	0.01	23.11	36.41	5.50	4.78	9.58	20.61

(c)

Element	C K	Al K	Mo L	Ag L	Ti K	Cr K	Ni K
Weight %	1.71	0.02	2.58	0.32	0.18	16.69	78.50

Fig. 4. 10 EDS analysis of regions (a) 1, (b) 2, and (c) 3 marked in FESEM micrograph of NANG illustrated as Fig 4.9 (d)

Table 4. 1 Specimen designation, composition, density, and microhardness

Designation	Composition	Real density (g/cm^3)	Microhardness HV$_{0.3}$ (GPa)
N0	Ni alloy	8.06	515 ± 5
NA	Ni alloy-10 wt.% Ag	8.46	496 ± 4
NAG	Ni alloy-10 wt.% Ag- 1 wt.% rGO	7.36	502 ± 6
NANG	Ni alloy-10 wt.% Ag-1 wt.% rGO-Ni	7.77	510 ± 3

4.1.2 Dry Sliding Friction and Wear

4.1.2.1 Variation of coefficient of friction with time

Figures. 4.11 (a-c) illustrate the variation in the CoF over time for N0, NA, NAG, and NANG at various temperatures (i.e., RT, 200, 400, 600, and 800 °C) under a constant normal load of 5 N and a fixed sliding speed of 0.5 m/s. All the materials have exhibited a stable variation with only marginal fluctuations in amplitude after attaining the steady state, depending upon the composition at all the temperatures except 800 °C, as seen in Figs. 4.11 (a and b). At RT, the CoF for N0 stabilizes after 168 seconds and remains constant until the completion of the test. In contrast, the CoFs for NA, NAG, and NANG stabilize after initial running-in period of 227, 282, and 180 seconds, respectively, with relatively smaller fluctuations as seen in Fig. 4.11 (a). At 200 °C, the CoF is found to stabilize after 420, 410, 204, and 192 seconds for N0, NA, NAG, and NANG, respectively, as shown in Fig. 4.11 (b). Similarly, at 400 °C, the CoF has been observed to stabilize after 46, 241, 173, and 520 seconds for N0, NA, NAG, and NANG, respectively as depicted in Fig. 4.11 (c). At 600 °C, the CoF is found to stabilize after 420, 230, 210, and 410 seconds, for N0, NA, NAG, and NANG, respectively as shown in Fig. 4.11 (d). At 800 °C, the CoFs for N0 and NA (Fig. 4.11 (e)) have been observed to stabilize after a short running-in period of 362 and 166 seconds, respectively, with relatively larger fluctuations than at temperature below 800 °C. However, both NAG and NANG have revealed a slightly increasing trend of variation in CoF with increasing duration of sliding.

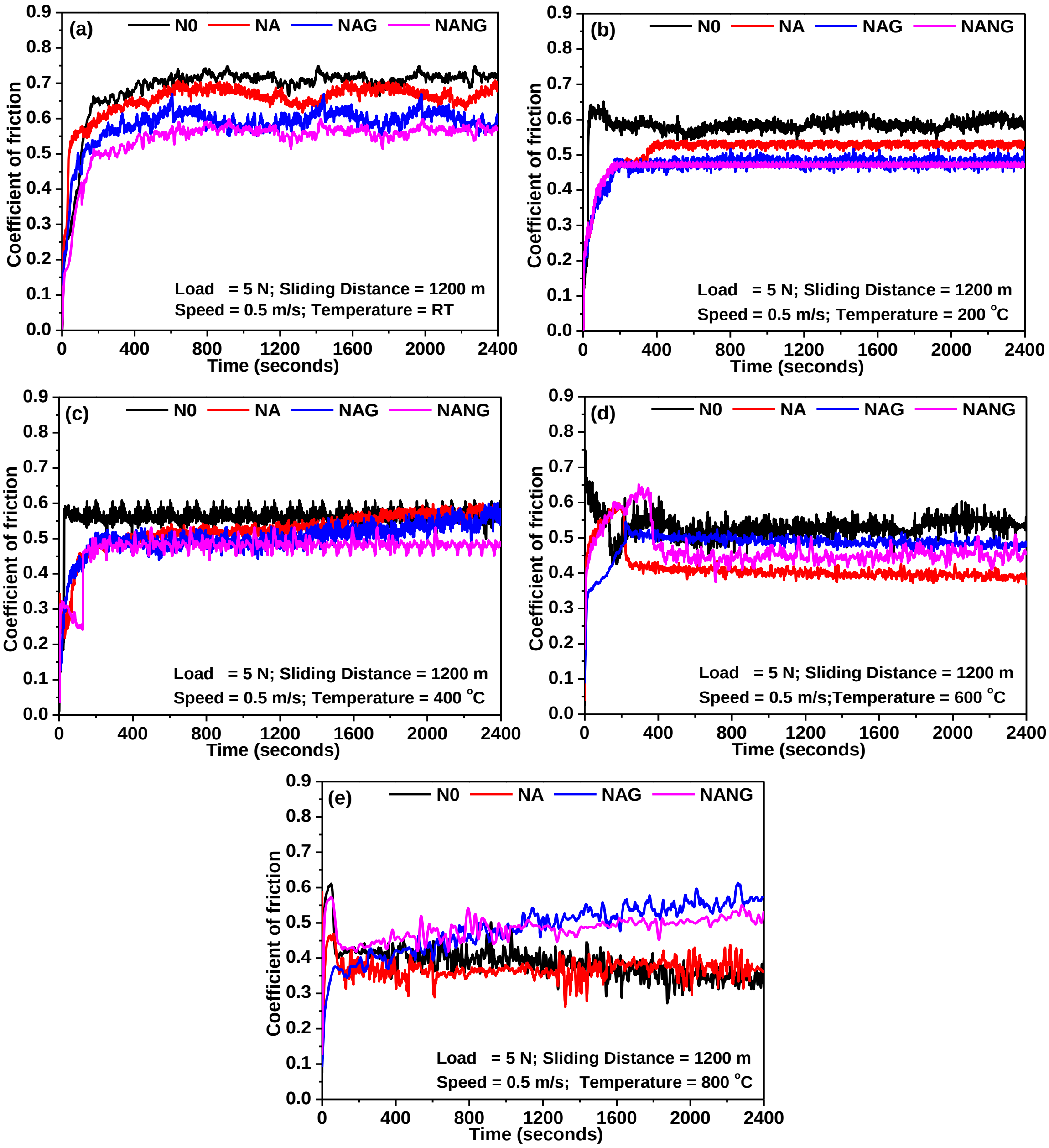

Fig. 4. 11 Variation of coefficient of friction with time at (a) RT, (b) 200, (c) 400, (d) 600, and (e) 800 °C for N0, NA, NAG, and NANG

4.1.2.2 Variation of average coefficient of friction with temperature

The average coefficient of friction for base alloy and composites has been estimated by discarding the duration of the running-in state. Figure 4.12 illustrates the variation of average CoF with temperature for N0, NA, NAG, and NANG. One may observe that the average CoF for N0 undergoes a decrease from RT to 200 °C, remains nearly constant between 200 and 600 °C, and then drops significantly from 600 to 800 °C. A similar trend of variation in average CoF has also been observed for NA, containing 10 wt.% Ag. However, NA has shown a relatively lower average CoF at all temperatures than base alloy, i.e., N0. The average CoF for NAG decreases from RT to 200 °C, which is followed by a marginal rise from 200 to 400 °C. However, it is observed to remain constant between 400 and 600 °C before increasing slightly at 800 °C. It may also be noted that NAG has a lower CoF than N0 and NA from RT to 600 °C and a higher average CoF at 800 °C. The CoF for NANG decreases sharply from RT to 200 °C, followed by an abrupt rise at 400 °C, remains stable till 600 °C, and increases thereafter at 800 °C. Among all the materials, NANG has shown the lowest CoF from RT to 600 °C. However, it has shown a comparatively higher CoF than N0 and NA at 800 °C.

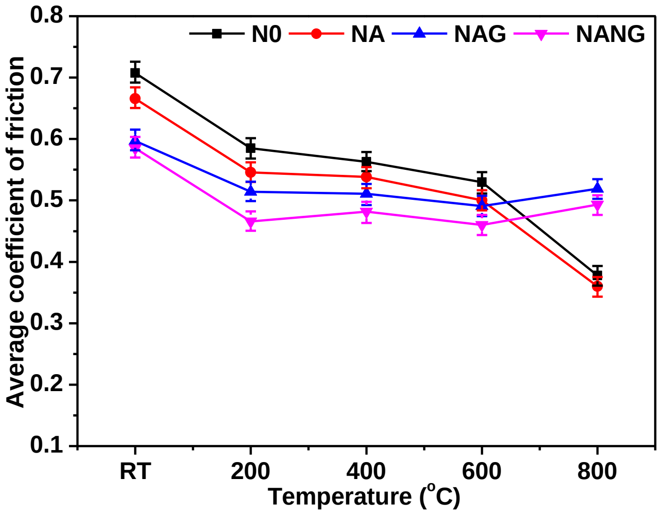

Fig. 4. 12 Variation of average coefficient of friction for base alloy and composites with temperature

4.1.2.3 Variation of wear rate with temperature

Figure 4.13 demonstrates the variation of specific wear rate with temperature for N0, NA, NAG, and NANG. The wear rate for N0 has been observed to increase with increasing temperature from RT to 600 °C followed by a decrease beyond that, whereas the same for NA has been found to increase from RT and 400 °C and a decrease thereafter till 800 °C. However, NA has shown a lower wear rate at all temperatures than base alloy, i.e., N0. The wear rate for NAG increases slightly from RT to 200 °C, which is followed by a marginal decrease at 400 °C. However, a significant decrease in wear rate could be observed from 400 to 800 °C. The wear rate NAG has been found to lie between N0 and NA at all temperatures. The wear rate for NANG increases marginally from RT to 200 °C and decreases thereafter till 600 °C before increasing again at 800 °C. However, NANG has shown the lowest wear rate compared to other composites at all temperatures except at 800 °C.

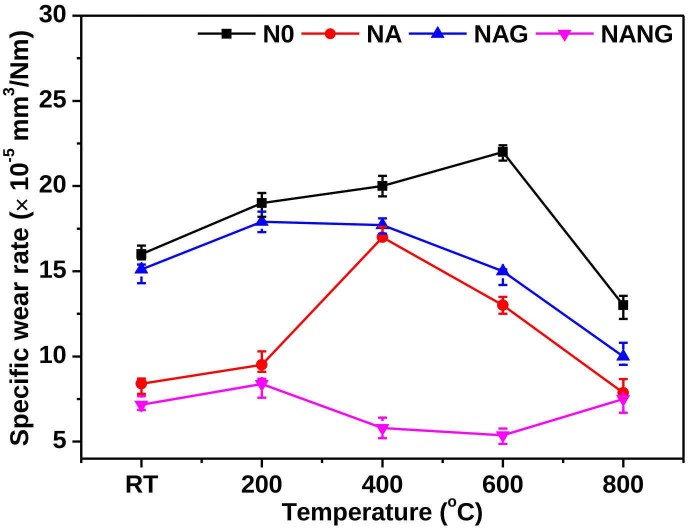

Fig. 4. 13 Variation of specific wear rate for base alloy and composites with temperature

4.1.3 Analysis of Worn Surfaces

4.1.3.1 Electron microscopy of worn surfaces of tribo-pair

The FESEM micrographs of the worn surfaces of N0 at RT, 200, 400, 600, and 800 °C, along with their EDS analyses, are shown in Figs. 4.14 (a-j). The worn surface of N0 at RT (Fig. 4.14 (a)) shows the presence of ploughing marks along with a transfer layer of wear debris, whereas the relatively shallow ploughing marks apart from a transfer layer can be seen on surface of N0 at 200 °C (Figs. 4.14 (c)) as compared to RT. A scattered transfer layer is observed on the worn surface at 400 °C (Fig. 4.14 (e)) with no visible sign of ploughing marks. One may also observe the presence of a scattered transfer layer on the surface worn at 600 °C (Fig. 4.14 (g)) with relatively smaller area coverage as compared to that at 400 °C as evident from a comparison of Figs. 4.14 (e and g). However, at 800 °C, a smooth and compacted transfer layer with no discernible ploughing marks could be observed on the worn surface of N0 as seen from Fig. 4.14 (i). EDS analyses of the square regions marked in Figs. 4.14 (a, c, e, g, and i) reveal the presence of constituent elements of the base alloy and oxygen along with their respective amounts depending on the temperature, indicating the possibility of oxidation as evident from EDS shown in Figs. 4.14 (b, d, f, h, and j).

The FESEM micrographs of the Si_3N_4 ball slid against N0 along with their EDS analyses at RT, 200, 400, 600, and 800 °C are shown in Figs. 4.15 (a-j). The worn surface of the ball slid against N0 at RT shows the presence of loose wear particles (Fig. 4.15 (a)), whereas, at 200 °C, the wear debris appears to be accumulated at the leading edge of ball (Fig. 4.15 (c)). The presence of a plateau of wear debris could be observed on the worn surface of the ball at 400 °C as seen in Fig 4.15 (e). The existence of a scattered transfer layer with moderate level of compaction is seen on the surface of the ball worn at 600 °C as shown in Fig. 4.15 (g), whereas a relatively smooth and compact transfer layer is observed on the surface of the ball worn at 800 °C as seen from Fig. 4.15 (i). EDS analysis of the regions marked by squares on the worn surface of the ball given in Figs. 4.15 (b, d, f, h, and j) reveal the transfer of material from the specimen to the ball, and the presence of oxygen points towards the oxidation of elements.

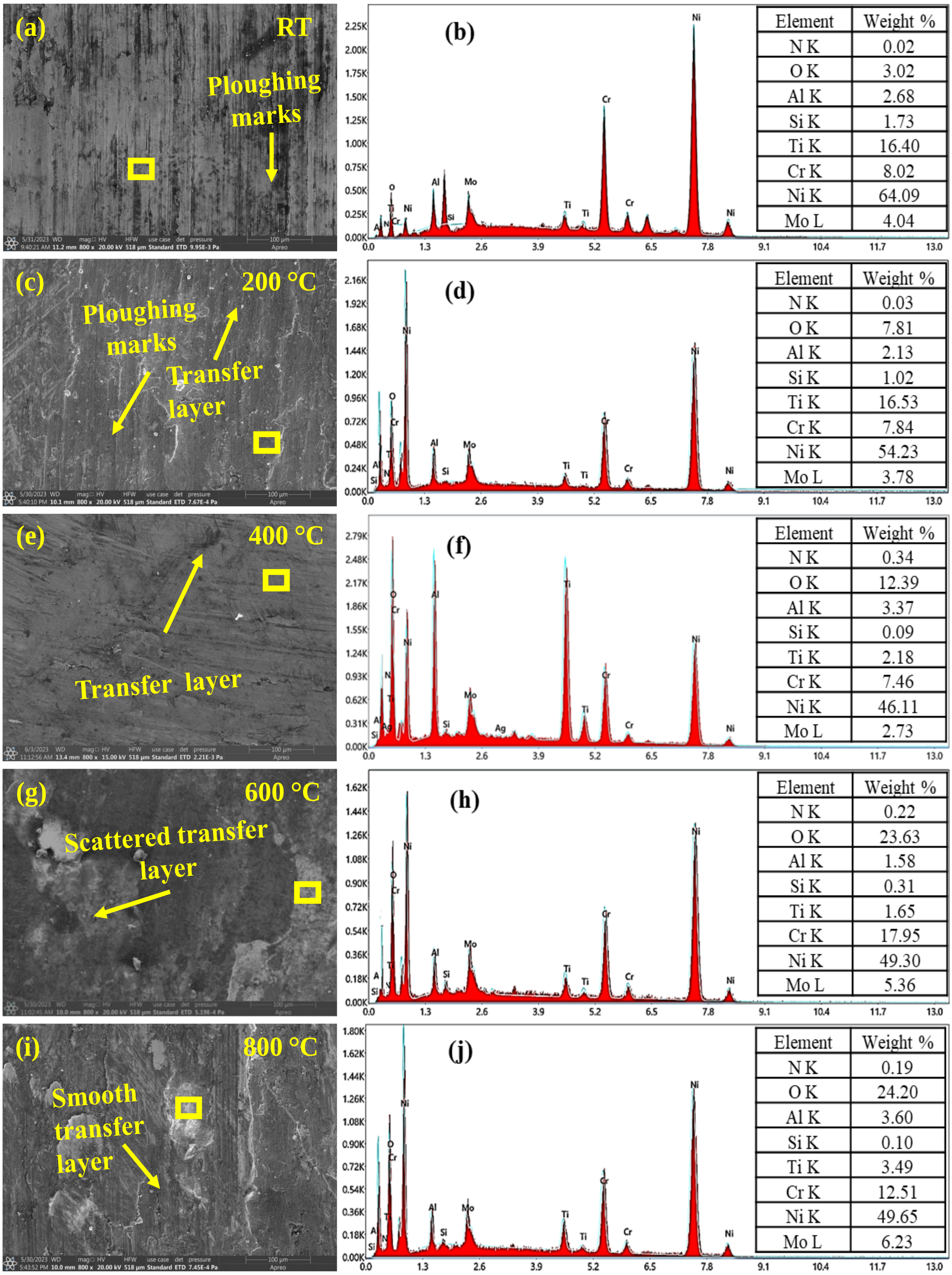

(b)

Element	Weight %
N K	0.02
O K	3.02
Al K	2.68
Si K	1.73
Ti K	16.40
Cr K	8.02
Ni K	64.09
Mo L	4.04

(d)

Element	Weight %
N K	0.03
O K	7.81
Al K	2.13
Si K	1.02
Ti K	16.53
Cr K	7.84
Ni K	54.23
Mo L	3.78

(f)

Element	Weight %
N K	0.34
O K	12.39
Al K	3.37
Si K	0.09
Ti K	2.18
Cr K	7.46
Ni K	46.11
Mo L	2.73

(h)

Element	Weight %
N K	0.22
O K	23.63
Al K	1.58
Si K	0.31
Ti K	1.65
Cr K	17.95
Ni K	49.30
Mo L	5.36

(j)

Element	Weight %
N K	0.19
O K	24.20
Al K	3.60
Si K	0.10
Ti K	3.49
Cr K	12.51
Ni K	49.65
Mo L	6.23

Fig. 4. 14 FESEM micrographs of the worn-out base alloy (N0) and EDS of the marked region at (a and b) RT, (c and d) 200, (e and f) 400, (g and h) 600, and (i and j) 800 °C

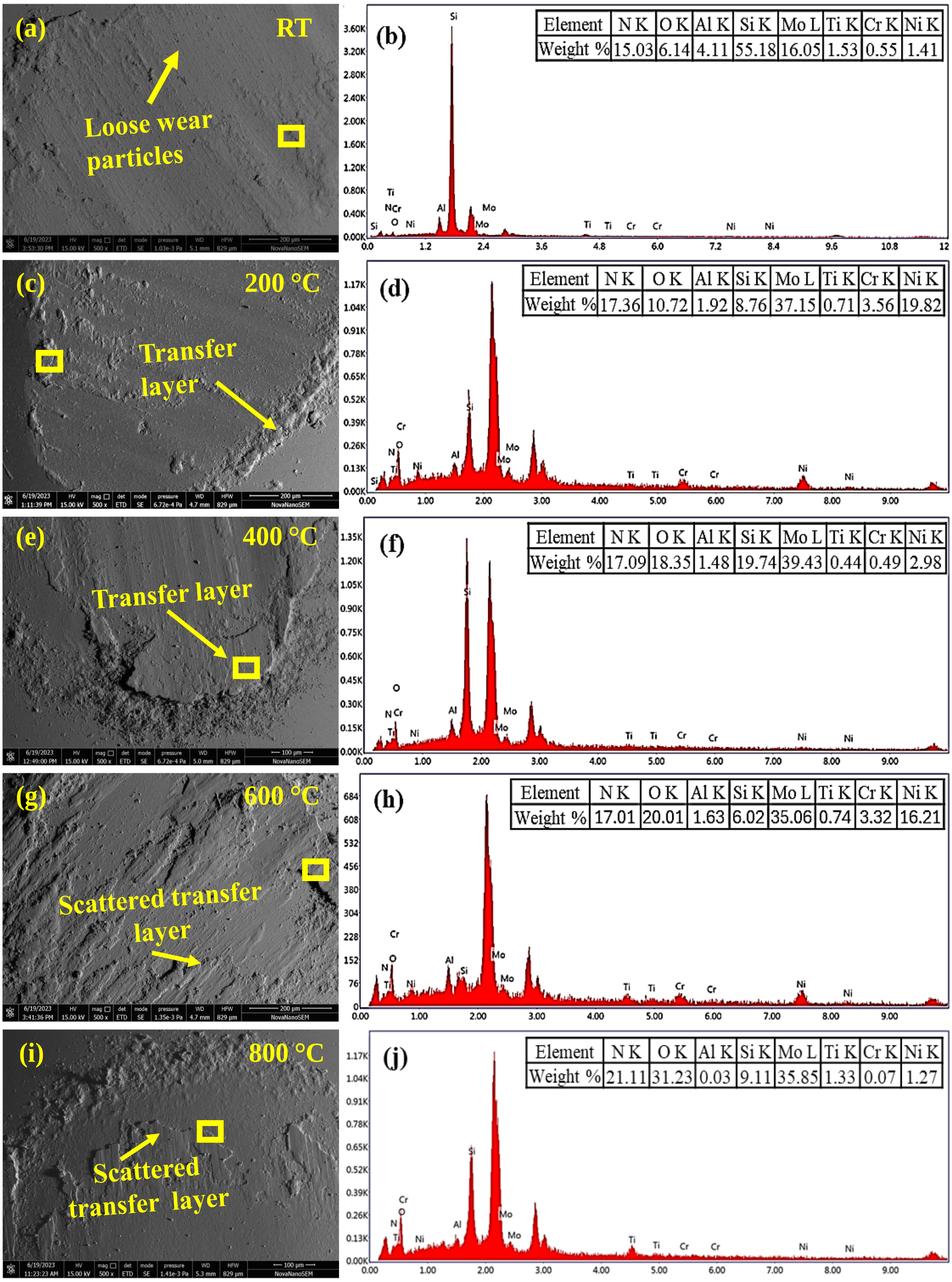

(b)

Element	N K	O K	Al K	Si K	Mo L	Ti K	Cr K	Ni K
Weight %	15.03	6.14	4.11	55.18	16.05	1.53	0.55	1.41

(d)

Element	N K	O K	Al K	Si K	Mo L	Ti K	Cr K	Ni K
Weight %	17.36	10.72	1.92	8.76	37.15	0.71	3.56	19.82

(f)

Element	N K	O K	Al K	Si K	Mo L	Ti K	Cr K	Ni K
Weight %	17.09	18.35	1.48	19.74	39.43	0.44	0.49	2.98

(h)

Element	N K	O K	Al K	Si K	Mo L	Ti K	Cr K	Ni K
Weight %	17.01	20.01	1.63	6.02	35.06	0.74	3.32	16.21

(j)

Element	N K	O K	Al K	Si K	Mo L	Ti K	Cr K	Ni K
Weight %	21.11	31.23	0.03	9.11	35.85	1.33	0.07	1.27

Fig. 4. 15 FESEM micrographs of the worn-out silicon nitride ball (counterface) slid against N0 along with EDS at the marked region at (a and b) RT, (c and d) 200, (e and f) 400, (g and h) 600, and (i and j) 800 °C

Figures 4.16 (a-j) illustrate the morphology of the worn surfaces of the NA after the tribo-tests at RT, 200, 400, 600, and 800 °C, along with their EDS analyses. The worn surface of NA at RT (Fig. 4.16 (a)) shows a smooth surface with fine ploughing marks along with some adhered wear particles, whereas the worn surfaces at 200 and 400 °C (Figs. 4.16 (c and e)) reveal the presence of a scattered transfer layer with different degrees of compaction and signs of delamination at 400 °C at a few places. The worn surface of NA at 600 °C depicted in Fig. 4.16 (g) exhibits the presence of a smooth and continuous transfer layer. However, at 800 °C, a smooth and well-compacted transfer layer covering nearly the entire area of the worn surface could be observed as seen in Fig. 4.16 (i). EDS analyses of the square regions marked in Figs. 4.16 (a, c, e, g, and i) show the existence of constituent elements of the composite and oxygen along with their respective amounts depending on the temperature, indicating the possibility of oxidation as evident from EDS shown in Figs. 4.16 (b, d, f, h, and j).

The FESEM micrographs of the Si_3N_4 ball slid against NA at RT, 200, 400, 600, and 800 °C, along with the EDS analyses, are shown Figs. 4.17 (a-j). The worn surface of the ball slid against NA at RT shows the presence of loose wear particles (Fig. 4.17 (a)) whereas, at 200 and 400 °C, the worn surfaces depict the presence of a plateau of wear debris on the worn surfaces of the ball as seen from Figs. 4.17 (c and e). The accumulation of the wear debris can be seen at the leading edge of ball on the surface of the ball worn at 600 °C as shown in Fig. 4.17 (g). However, a smooth and compact transfer layer can be seen on the worn surface of the ball at 800 °C as depicted in Fig. 4.17 (i). EDS analysis of the regions marked by squares on the worn surface of the ball given in Figs. 4.17 (b, d, f, h, and j) reveal the transfer of material from the composite to the ball, and the presence of oxygen points towards the oxidation of elements.

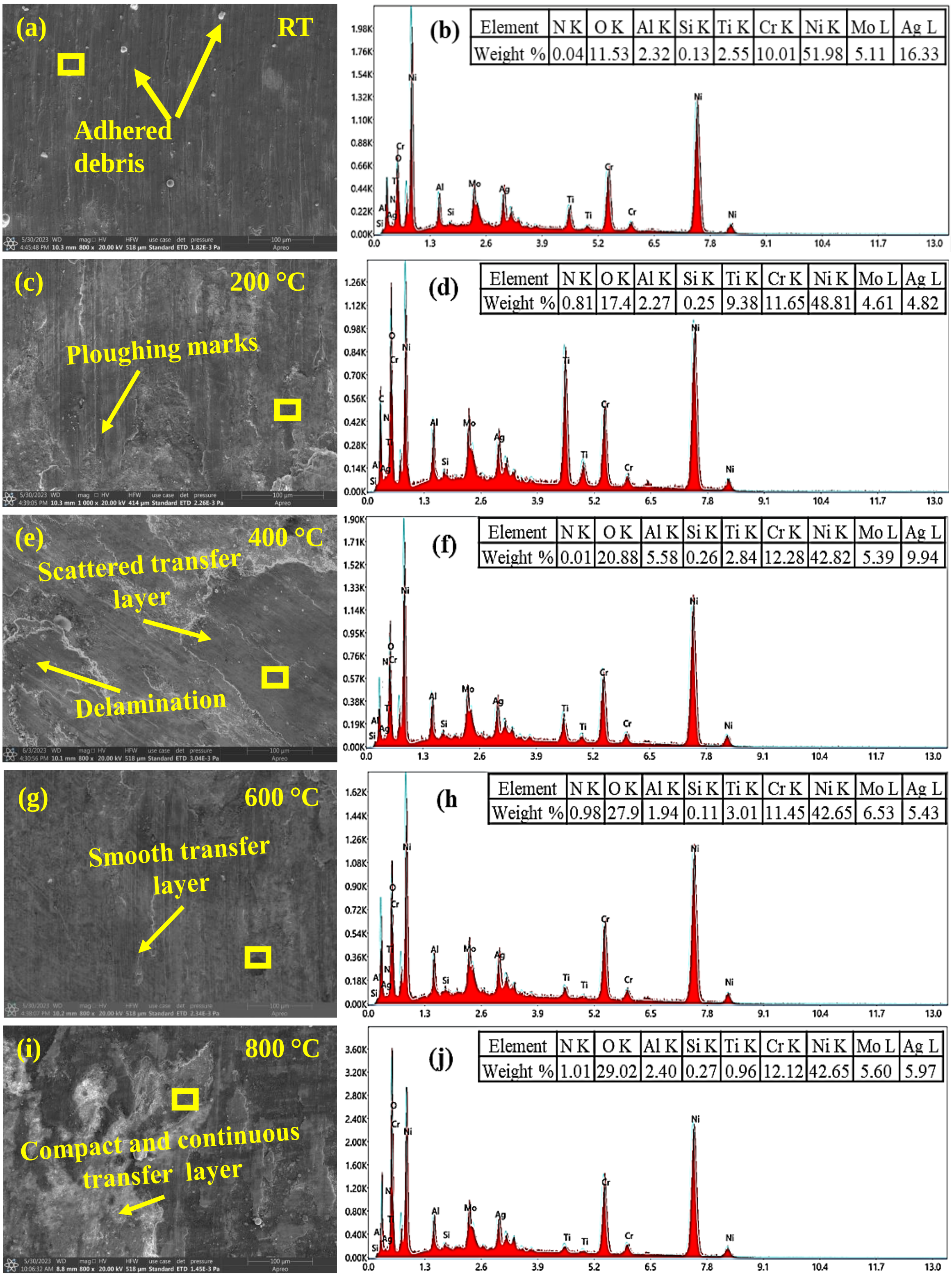

(b)

Element	N K	O K	Al K	Si K	Ti K	Cr K	Ni K	Mo L	Ag L
Weight %	0.04	11.53	2.32	0.13	2.55	10.01	51.98	5.11	16.33

(d)

Element	N K	O K	Al K	Si K	Ti K	Cr K	Ni K	Mo L	Ag L
Weight %	0.81	17.4	2.27	0.25	9.38	11.65	48.81	4.61	4.82

(f)

Element	N K	O K	Al K	Si K	Ti K	Cr K	Ni K	Mo L	Ag L
Weight %	0.01	20.88	5.58	0.26	2.84	12.28	42.82	5.39	9.94

(h

Element	N K	O K	Al K	Si K	Ti K	Cr K	Ni K	Mo L	Ag L
Weight %	0.98	27.9	1.94	0.11	3.01	11.45	42.65	6.53	5.43

(j)

Element	N K	O K	Al K	Si K	Ti K	Cr K	Ni K	Mo L	Ag L
Weight %	1.01	29.02	2.40	0.27	0.96	12.12	42.65	5.60	5.97

Fig. 4. 16 FESEM micrographs of the worn-out NA and EDS of the marked region at (a and b) RT, (c and d) 200, (e and f) 400, (g and h) 600, and (i and j) 800 °C

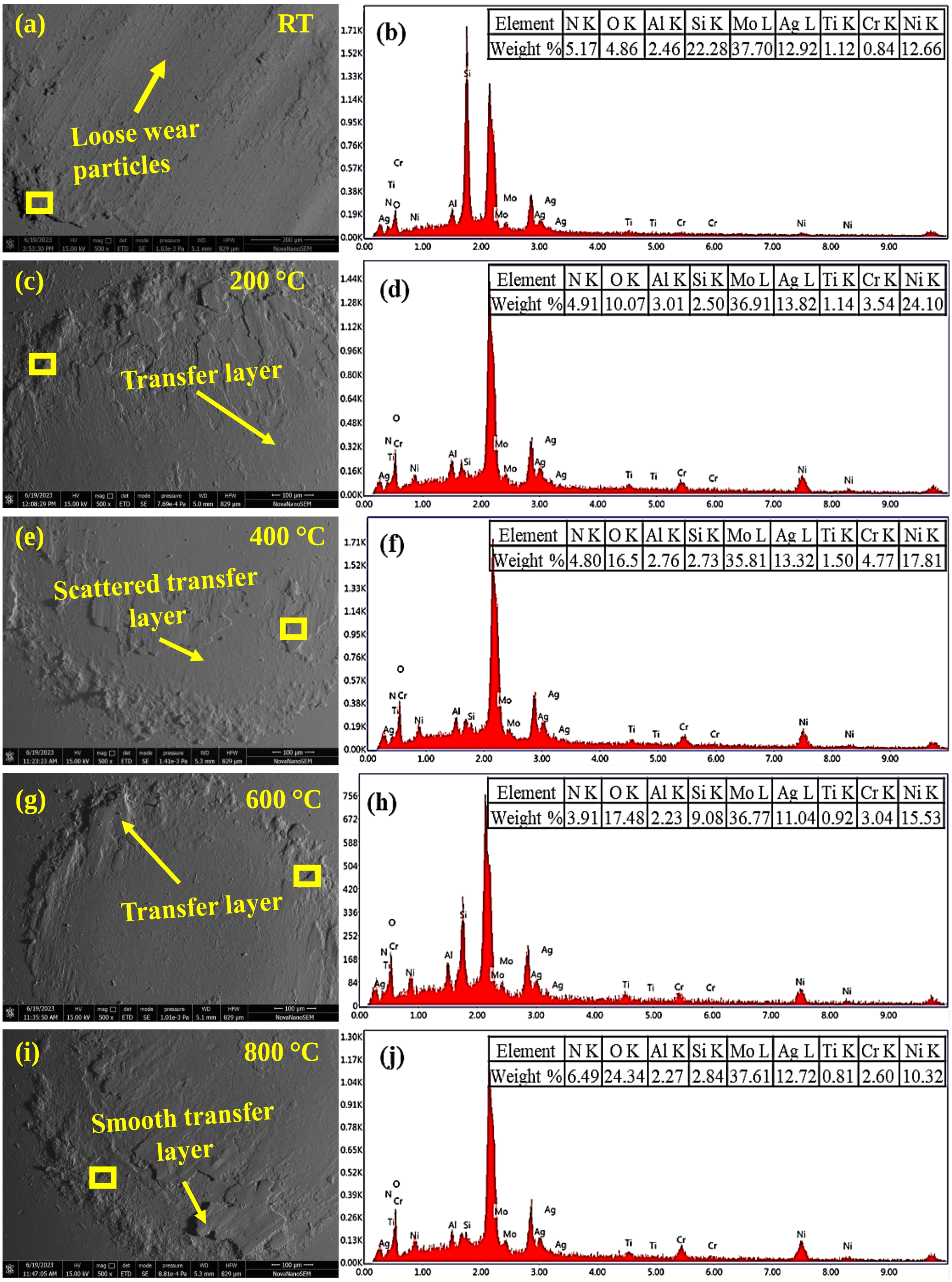

(b)

Element	N K	O K	Al K	Si K	Mo L	Ag L	Ti K	Cr K	Ni K
Weight %	5.17	4.86	2.46	22.28	37.70	12.92	1.12	0.84	12.66

(d)

Element	N K	O K	Al K	Si K	Mo L	Ag L	Ti K	Cr K	Ni K
Weight %	4.91	10.07	3.01	2.50	36.91	13.82	1.14	3.54	24.10

(f)

Element	N K	O K	Al K	Si K	Mo L	Ag L	Ti K	Cr K	Ni K
Weight %	4.80	16.5	2.76	2.73	35.81	13.32	1.50	4.77	17.81

(h)

Element	N K	O K	Al K	Si K	Mo L	Ag L	Ti K	Cr K	Ni K
Weight %	3.91	17.48	2.23	9.08	36.77	11.04	0.92	3.04	15.53

(j)

Element	N K	O K	Al K	Si K	Mo L	Ag L	Ti K	Cr K	Ni K
Weight %	6.49	24.34	2.27	2.84	37.61	12.72	0.81	2.60	10.32

Fig. 4. 17 FESEM micrographs of the worn-out silicon nitride ball (counterface) slid against NA along with EDS at the marked region at (a and b) RT, (c and d) 200, (e and f) 400, (g and h) 600, and (i and j) 800 °C

The FESEM images of the worn surfaces of the NAG and counterface ball at RT, 200, 400, 600, and 800 °C, along with their EDS analyses, are depicted in Figs. 4.18 (a–j). The shallow ploughing marks covered with a transfer layer of wear debris could be observed on the worn surface of NAG at RT (Fig. 4.18 (a)), while a smooth and compact transfer layer with signs of delamination could be seen over the worn surface at 200 °C (Fig. 4.18 (c)). The existence of the transfer with delamination at some location can be seen on the worn surface at 400 °C as shown in Fig. 4.18 (e)). The presence of the transfer layer with no signs of delamination on the worn surface of NAG at 600 °C, as seen in Fig. 4.18 (g). At 800 °C, the worn surface of NAG reveals fine ploughing marks covered by a scattered transfer layer and loose wear particles, as evident from Fig. 4.18 (i). Again, the EDS analyses of the square regions marked on the worn surface of NAG as shown in Figs. 4.18 (a, c, e, g, and i) reveal the presence of constituent elements of the composite and oxygen as evident from Fig. 4.18 (b, d, f, h and j).

The FESEM micrographs of the Si_3N_4 ball slid against NAG at RT, 200, 400, 600, and 800 °C, along with the EDS analyses are shown Figs. 4.19 (a-j). The worn surface of the ball slid against NAG (Fig. 4.19 (a)) shows the presence of loose wear particles at RT, whereas the existence of the transfer layer of varying degrees of compactness can be observed on the worn surfaces of ball slid against NAG at 200 and 400 °C as depicted in Figs. 4.19 (c and e). One may observe the presence of a plateau of wear debris which appear to be spalling from worn surface of the ball at 600 °C as depicted in Fig. 4.19 (g). However, the presence of a well-compacted transfer layer of wear debris can be seen on the worn surface of the ball at 800 °C as evident from Fig. 4.19 (i). EDS analysis of the regions marked by squares on the worn surface of the ball given in Figs. 4.18(b, d, f, h, and j) reveal the transfer of material from the composite to the ball, and the presence of oxygen points towards the oxidation of elements.

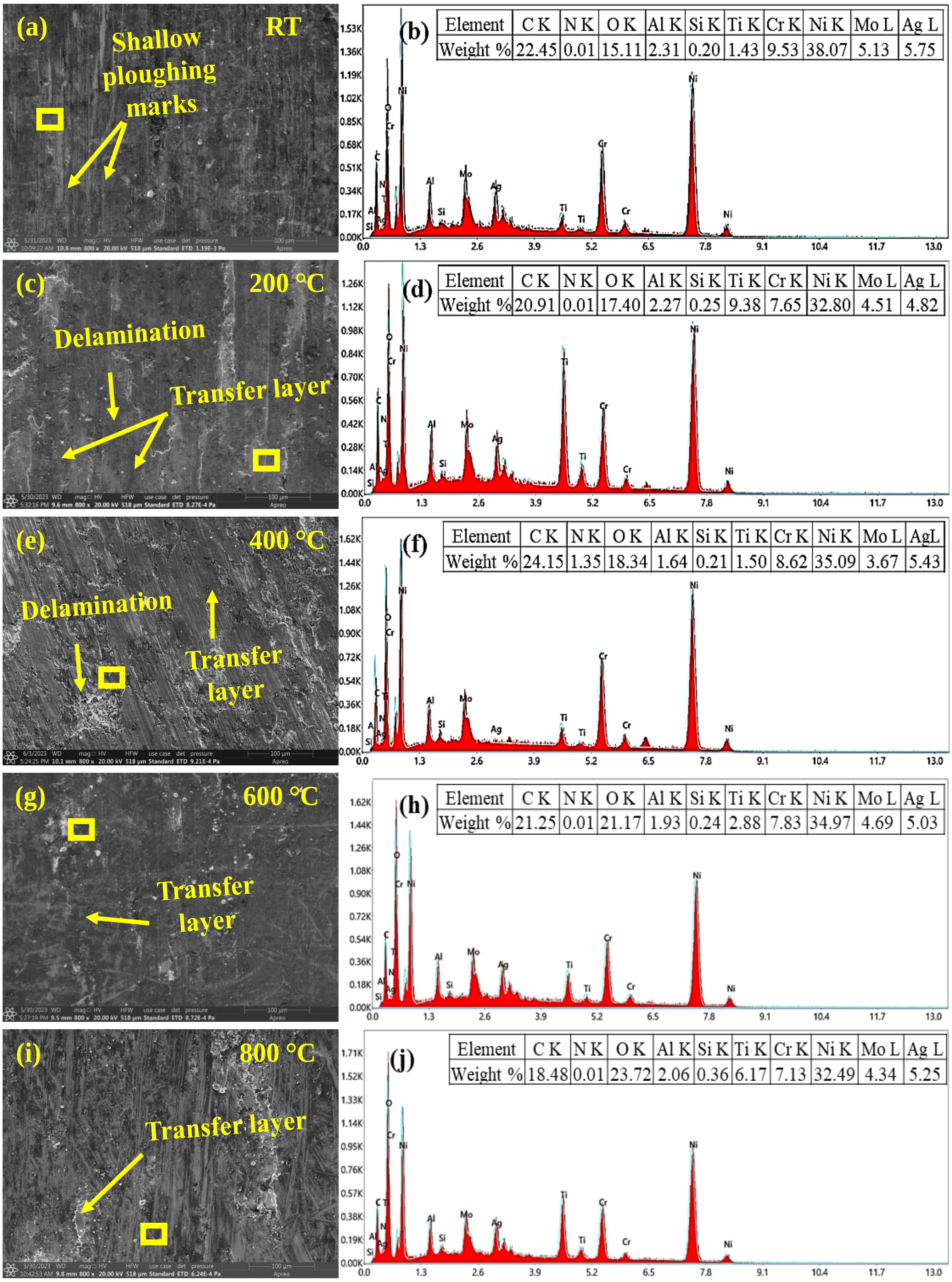

(b)

Element	C K	N K	O K	Al K	Si K	Ti K	Cr K	Ni K	Mo L	Ag L
Weight %	22.45	0.01	15.11	2.31	0.20	1.43	9.53	38.07	5.13	5.75

(d)

Element	C K	N K	O K	Al K	Si K	Ti K	Cr K	Ni K	Mo L	Ag L
Weight %	20.91	0.01	17.40	2.27	0.25	9.38	7.65	32.80	4.51	4.82

(f)

Element	C K	N K	O K	Al K	Si K	Ti K	Cr K	Ni K	Mo L	AgL
Weight %	24.15	1.35	18.34	1.64	0.21	1.50	8.62	35.09	3.67	5.43

(h)

Element	C K	N K	O K	Al K	Si K	Ti K	Cr K	Ni K	Mo L	Ag L
Weight %	21.25	0.01	21.17	1.93	0.24	2.88	7.83	34.97	4.69	5.03

(j)

Element	C K	N K	O K	Al K	Si K	Ti K	Cr K	Ni K	Mo L	Ag L
Weight %	18.48	0.01	23.72	2.06	0.36	6.17	7.13	32.49	4.34	5.25

Fig. 4. 18 FESEM micrographs of the worn-out NAG and EDS of the marked region at (a and b) RT, (c and d) 200, (e and f) 400, (g and h) 600, and (i and j) 800 °C

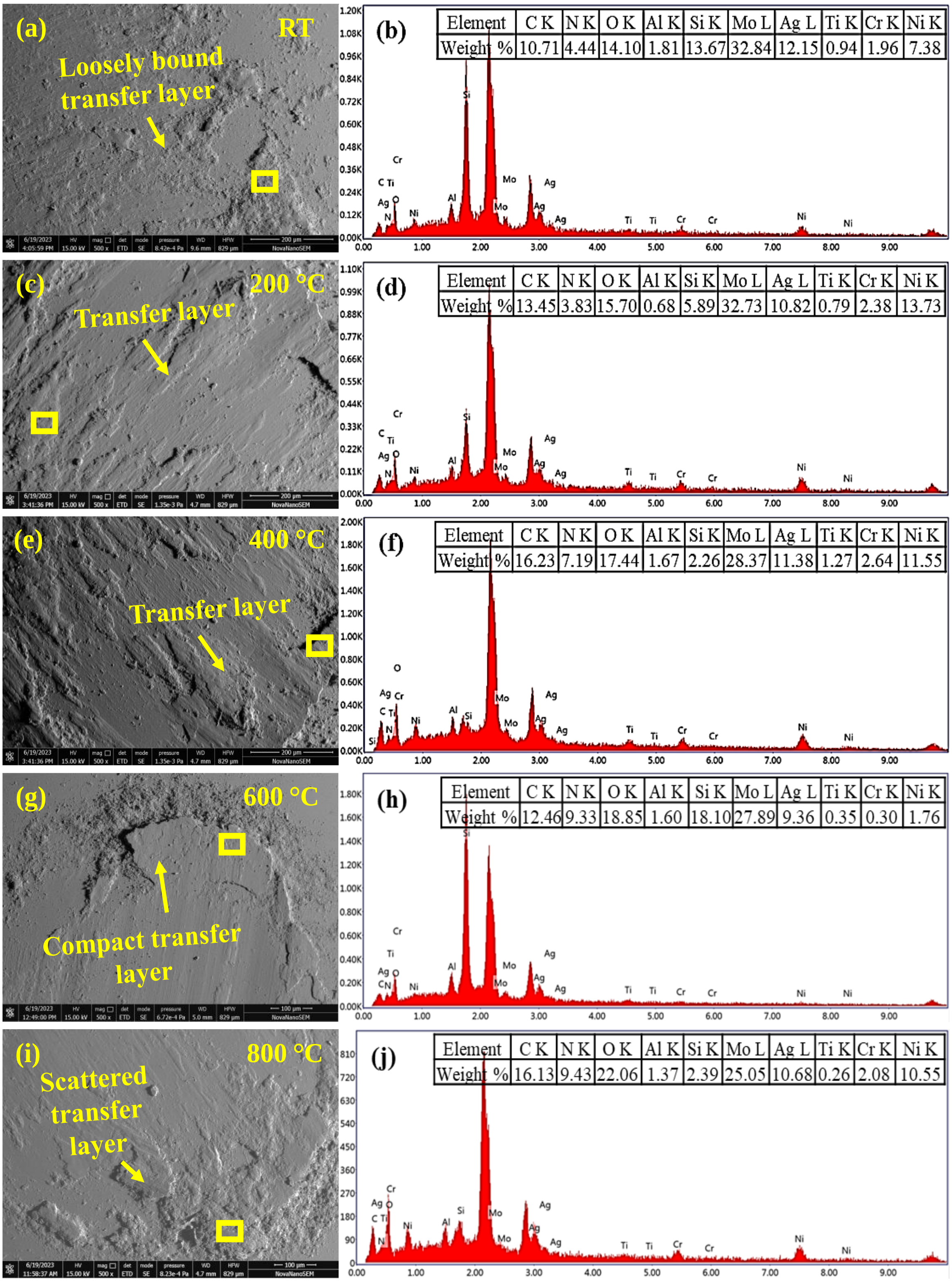

(b)

Element	C K	N K	O K	Al K	Si K	Mo L	Ag L	Ti K	Cr K	Ni K
Weight %	10.71	4.44	14.10	1.81	13.67	32.84	12.15	0.94	1.96	7.38

(d)

Element	C K	N K	O K	Al K	Si K	Mo L	Ag L	Ti K	Cr K	Ni K
Weight %	13.45	3.83	15.70	0.68	5.89	32.73	10.82	0.79	2.38	13.73

(f)

Element	C K	N K	O K	Al K	Si K	Mo L	Ag L	Ti K	Cr K	Ni K
Weight %	16.23	7.19	17.44	1.67	2.26	28.37	11.38	1.27	2.64	11.55

(h)

Element	C K	N K	O K	Al K	Si K	Mo L	Ag L	Ti K	Cr K	Ni K
Weight %	12.46	9.33	18.85	1.60	18.10	27.89	9.36	0.35	0.30	1.76

(j)

Element	C K	N K	O K	Al K	Si K	Mo L	Ag L	Ti K	Cr K	Ni K
Weight %	16.13	9.43	22.06	1.37	2.39	25.05	10.68	0.26	2.08	10.55

Fig. 4. 19 FESEM micrographs of the worn-out silicon nitride ball (counterface) slid against NAG along with EDS at the marked region at (a and b) RT, (c and d) 200, (e and f) 400, (g and h) 600, and (i and j) 800 °C

The FESEM micrographs of the worn surfaces of NANG and the corresponding Si_3N_4 ball slid at RT, 200, 400, 600, and 800 °C, and their EDS analyses are shown in Figs. 4.20 (a-j). The shallow ploughing marks covered with a scattered transfer layer could be clearly observed on the worn surface of NANG at RT (Fig. 4.20 (a)), while a smooth and compacted transfer layer covering the entire worn surface could be seen at 200 °C (Fig. 4.20 (c)). The existence of a smooth transfer layer with some loose wear debris can be seen on the surface of NANG worn at 400 °C as shown in Fig. 4.20 (e). At 600 °C, the worn surface of NANG shows the presence of a compacted transfer layer with detachments from a few locations, as seen in Fig. 4.20 (g). The worn surface of NANG illustrated in Fig. 4.20 (i) shows the presence of shallow ploughing marks covered by a scattered layer of wear debris at 800 °C. Again, the EDS analyses of the square regions marked in Figs. 4.20 (a, c, e, g, and i) reveal the presence of constituent elements of the composite and oxygen as evident from Figs. 4.20 (b, d, f, h, and j).

The FESEM micrographs of the Si_3N_4 ball slid against NANG at RT, 200, 400, 600, and 800 °C, along with their EDS analyses are shown Figs. 4.21 (a-j). The worn surface of the ball at RT (Fig. 4.21 (a)) has revealed the presence of a loosely bound transfer layer of wear debris on the surface. The wear debris appears to have accumulated at the leading edge of the ball at 200 and 400 °C as shown in Figs. 4.21 (c and e). The existence of a plateau of wear debris can be seen on the worn surface of ball slid against NANG at 600 °C as depicted in Fig. 4.21 (g). However, at 800 °C, the presence of a plateau of wear debris can observe on the worn surface of ball which appears to be spalling from the surface as seen from Fig. 4.21 (i). Again, the EDS analyses of the square regions marked on the worn surface of ball slid against NANG as shown in Figs. 4.21 (a, c, e, g, and i) reveal the presence of constituent elements of the composite and oxygen as evident from Fig. 4.21 (b, d, f, h, and j).

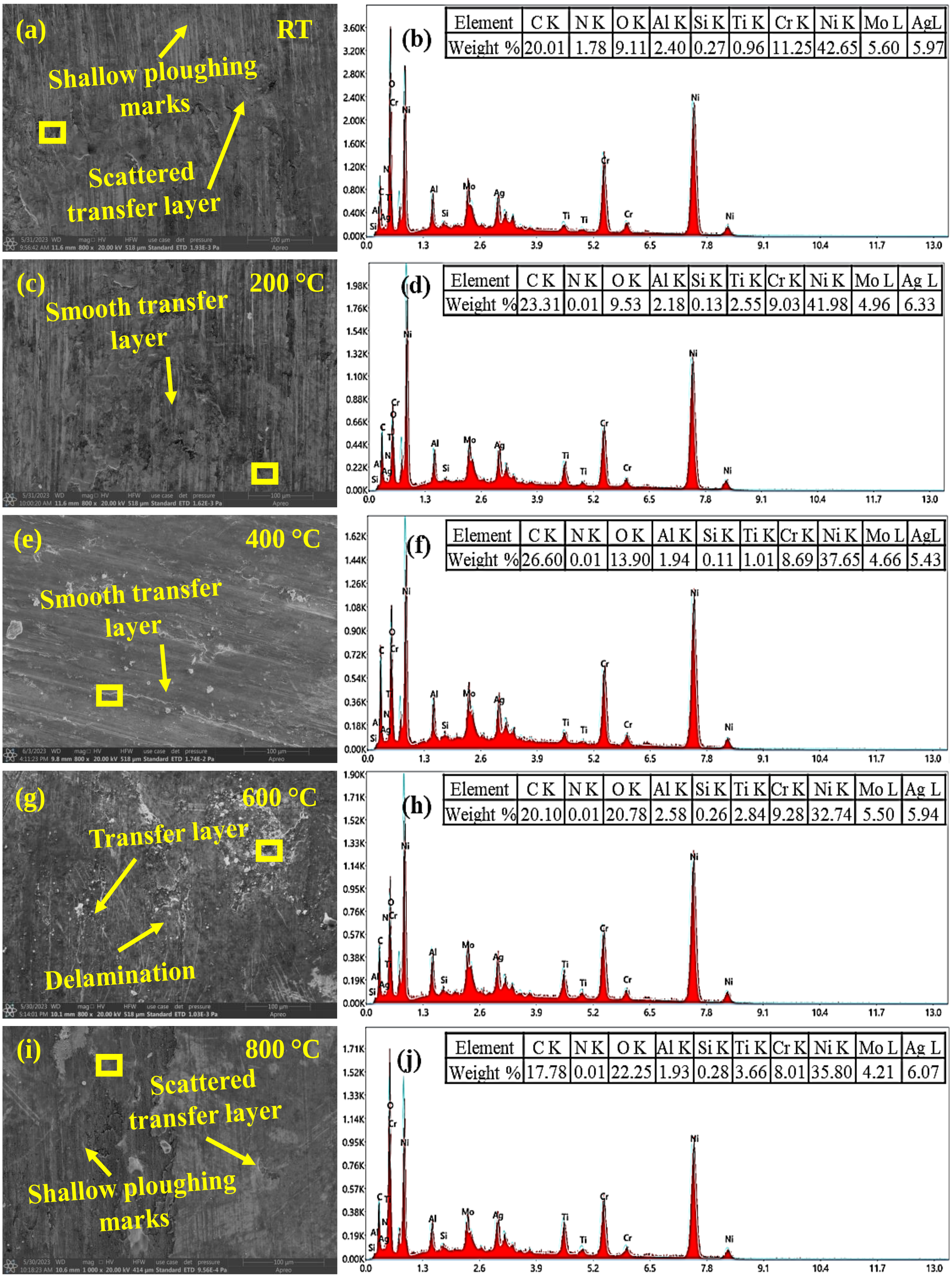

(b)

Element	C K	N K	O K	Al K	Si K	Ti K	Cr K	Ni K	Mo L	AgL
Weight %	20.01	1.78	9.11	2.40	0.27	0.96	11.25	42.65	5.60	5.97

(d)

Element	C K	N K	O K	Al K	Si K	Ti K	Cr K	Ni K	Mo L	Ag L
Weight %	23.31	0.01	9.53	2.18	0.13	2.55	9.03	41.98	4.96	6.33

(f)

Element	C K	N K	O K	Al K	Si K	Ti K	Cr K	Ni K	Mo L	AgL
Weight %	26.60	0.01	13.90	1.94	0.11	1.01	8.69	37.65	4.66	5.43

(h)

Element	C K	N K	O K	Al K	Si K	Ti K	Cr K	Ni K	Mo L	Ag L
Weight %	20.10	0.01	20.78	2.58	0.26	2.84	9.28	32.74	5.50	5.94

(j)

Element	C K	N K	O K	Al K	Si K	Ti K	Cr K	Ni K	Mo L	Ag L
Weight %	17.78	0.01	22.25	1.93	0.28	3.66	8.01	35.80	4.21	6.07

Fig. 4. 20 FESEM micrographs of the worn-out NANG and EDS of the marked region at (a and b) RT, (c and d) 200, (e and f) 400, (g and h) 600, and (i and j) 800 °C

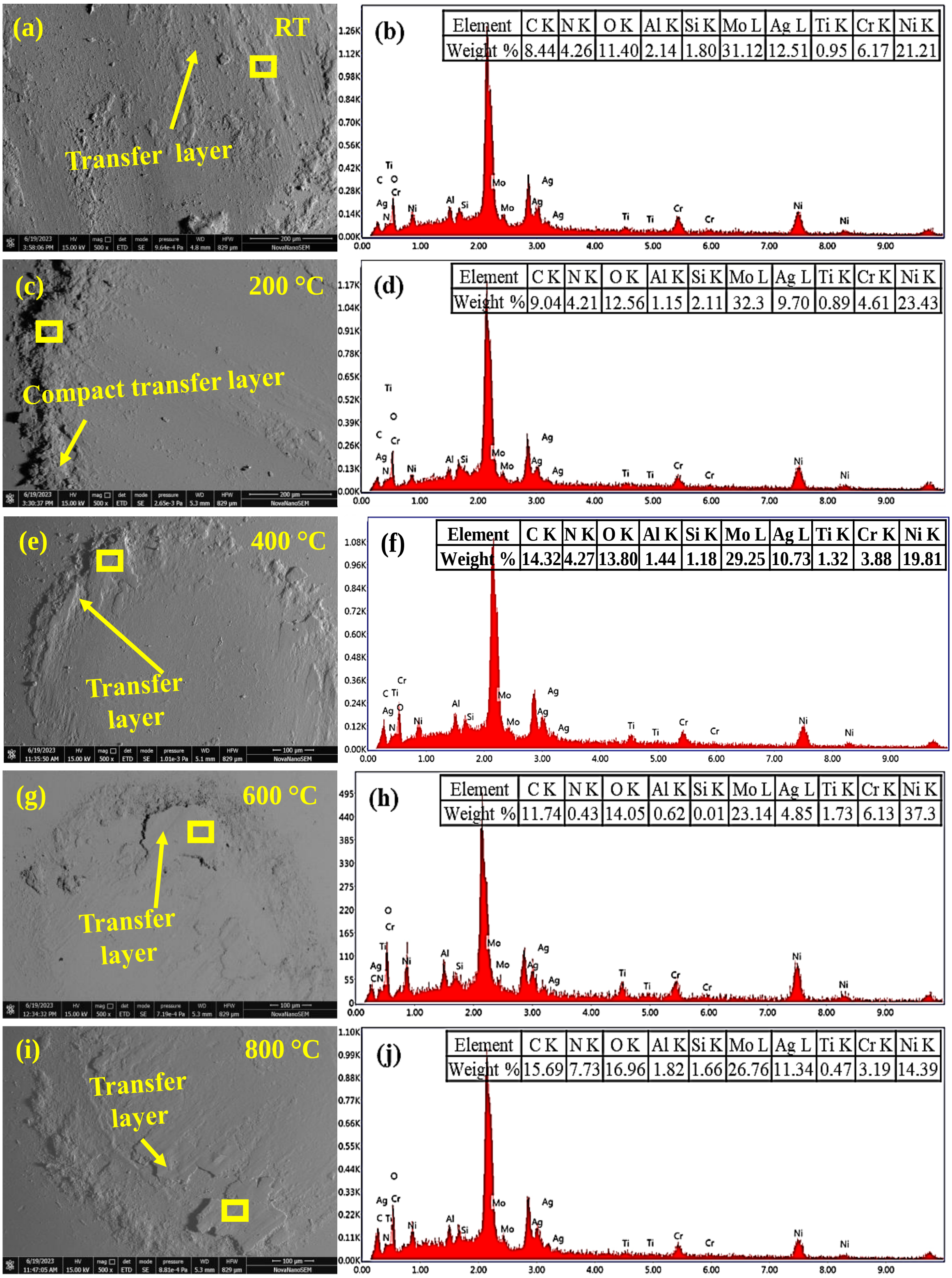

Fig. 4. 21 FESEM micrographs of the worn-out silicon nitride ball (counterface) slid against NANG along with EDS at the marked region at (a and b) RT, (c and d) 200, (e and f) 400, (g and h) 600, and (i and j) 800 °C.

4.1.3.2 X-ray diffraction analysis of worn surface of composites

The X-ray diffraction patterns of the worn surfaces of N0, NA, NAG, and NANG at various temperatures are given in Figs. 4.22 (a-d). The XRD pattern of the worn surface of N0 (Fig. 4.22 (a)) at RT reveals the presence of diffraction peaks corresponding to NiCr (ICSD 98-010-2819), NiAl (ICSD 98-060-4356), and NiTi (ICSD 98-016-6010). One may also observe an additional peak of MoO_3 (ICSD 00-021-0569) at 200 °C. However, the new peaks corresponding to NiO (ICSD 98-009-2129), $NiMoO_4$ (ICSD98-017-4488), and $NiTiO_3$ (ICSD 98-007-9285) could also be seen depending on the test temperature (400,600, and 800 °C) as seen in Fig. 4.22 (a). XRD patterns of NA illustrated in Fig. 4.22 (b) demonstrate the presence of some additional peaks of Ag (ICSD 01-087-0598), $Ag_2Mo_2O_7$ (ICSD 00-021-1339), Ag_2MoO_4 (ICSD 00-008-473) based on the temperature. XRD patterns of NAG and NANG illustrated in Figs. 4.22 (c and d) reveal extra peaks corresponding to Ni_6Mo_6C (ICSD 98-061-8328), MoC (ICSD 98-004-3523), and $Cr_{23}C_6$ (ICSD 98-006-2667) apart from those observed for NA depending on the temperature.

4.1.3.3 Raman analysis of the worn surface of the composites

The micro-Raman spectra of the worn surfaces of N0, NA, NAG, and NANG at different temperatures are presented in Fig. 4.23. The Raman spectrum of the worn surface of N0 (Fig. 4.23 (a)) at RT reveals the presence of diffraction peaks corresponding to Al_2O_3 only, whereas one additional peak of MoO_3 is visible at 200 °C. The peaks corresponding to NiO, Cr_2O_3, and $NiMoO_4$ could be seen at 400 °C along with those of Al_2O_3 and MoO_3. However, a new peak corresponding to $NiCr_2O_4$ could be seen at 600 and 800 °C apart from those observed at 400 °C. Raman spectra of NA, NAG and NANG illustrated in Figs. 4.23 (b-d) show the presence of similar peaks for N0 at all the temperatures. The additional peaks corresponding to $Ag_2Mo_2O_7$ and Ag_2MoO_4 could be seen in the Raman spectrum of

NA at 600 and 800°C. However, a peak corresponding to $Ag_2Mo_2O_7$ only, has been observed in Raman spectra of NAG and NANG.

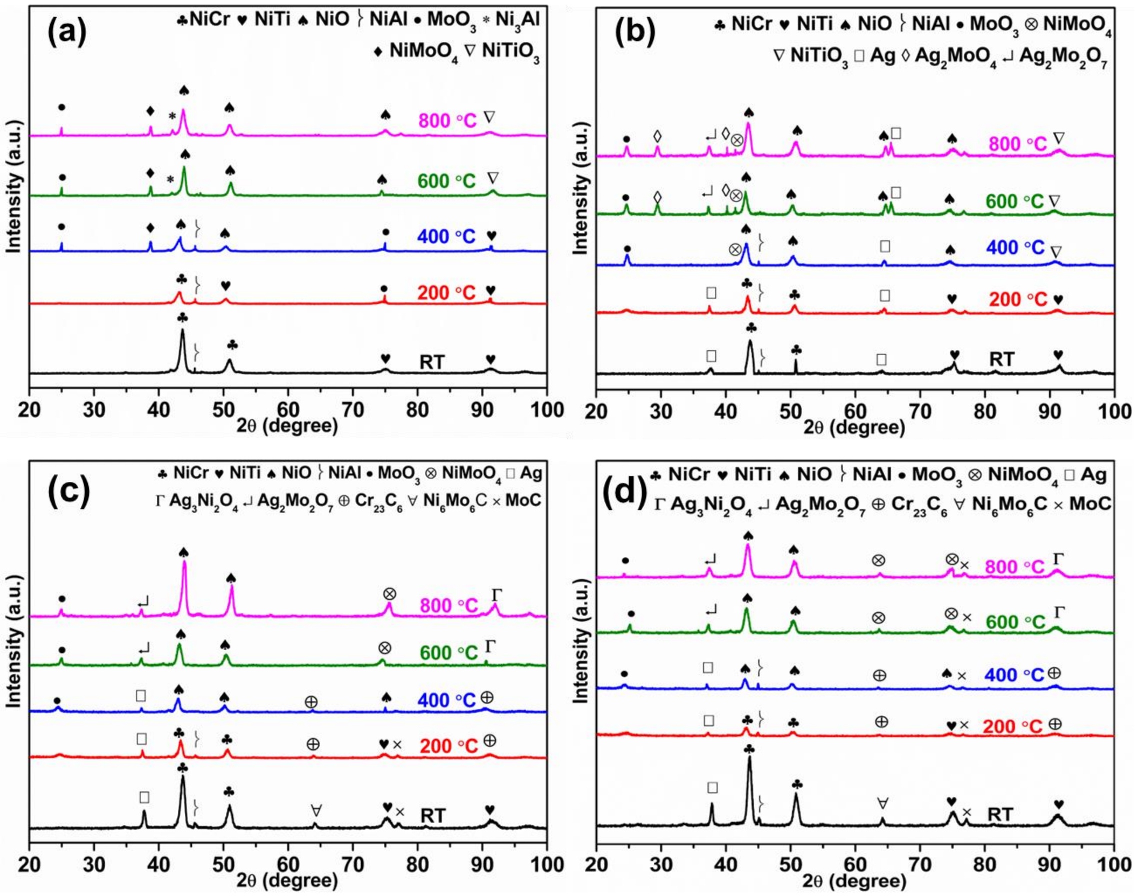

Fig. 4. 22 X -ray diffraction patterns of worn composite (a) N0 (b) NA, (c) NAG, and (d) NANG at all the temperatures

4.1.3.4 Examination of Subsurfaces

FESEM images of the subsurface for N0, NA, NAG, and NANG, worn at 800°C depicted in Figs. 4.24 (a-d) confirm the presence of a tribo-layer. The average thickness of tribo-layer for N0, NA, NAG, and NANG is 127.9, 137.4, 33.6, and 72.1 µm, respectively.

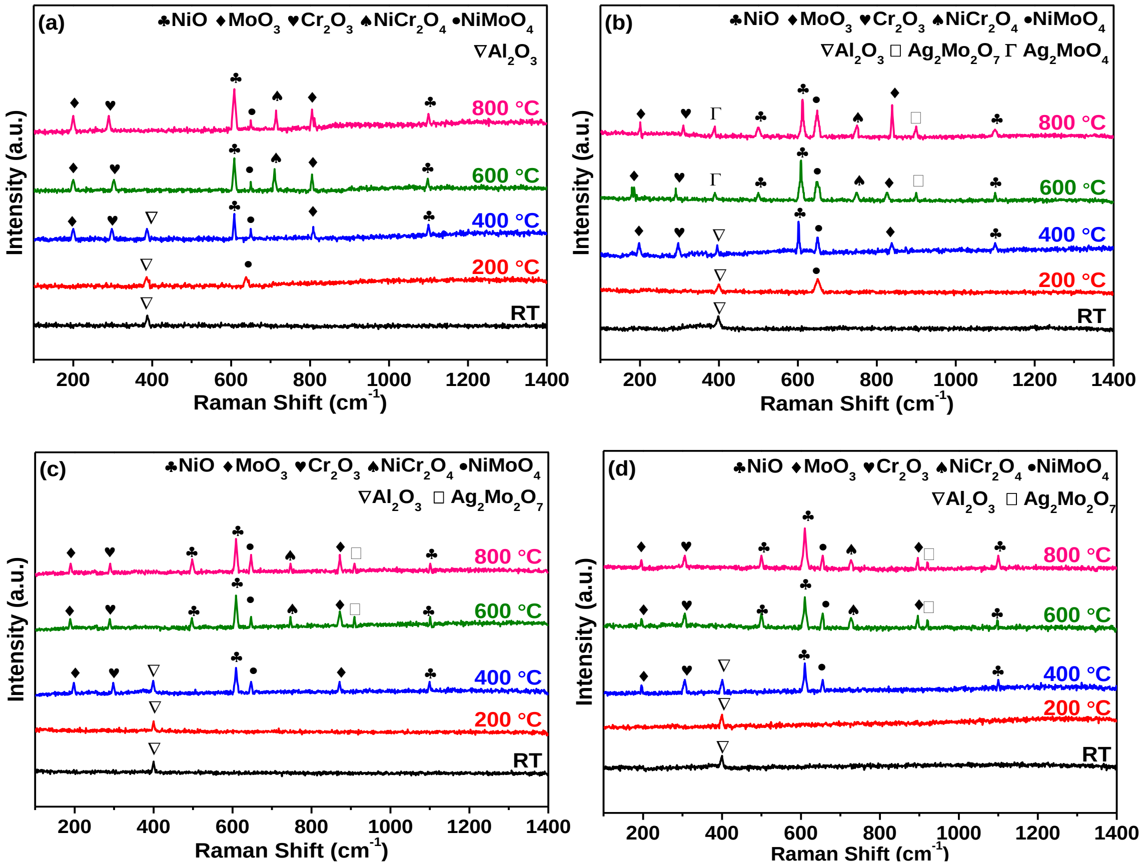

Fig. 4. 23 Raman spectra of worn surface of (a) N0, (b) NA, (c) NAG, and (d) NANG at different temperatures

4.2 DISCUSSION

The addition of either Ag or the combination of Ag and rGO, as well as Ag and rGO-Ni in the base alloy, i.e., N0, decreases the hardness of N0. The reduced hardness of NA compared to N0 may be attributed to the inherent softness of Ag, which has also been reported by others [39,67,94]. The relatively higher hardness of NAG compared to NA may be ascribed to the presence of a hard MoC phase as confirmed by the XRD analysis given in Fig. 4.8 (b). An increase in the hardness of Cu due to the presence of MoC in the Cu-rGO-MoS_2 composite has also been reported by Nautiyal et al. [55]. The increased hardness of NANG compared to NAG may be credited to the uniform distribution of rGO-Ni in the matrix, as seen from a comparison of Figs. 4.9 (c and d) due to the enhanced wetting characteristics of rGO-Ni with the matrix and this might also have contributed to increased hardness.

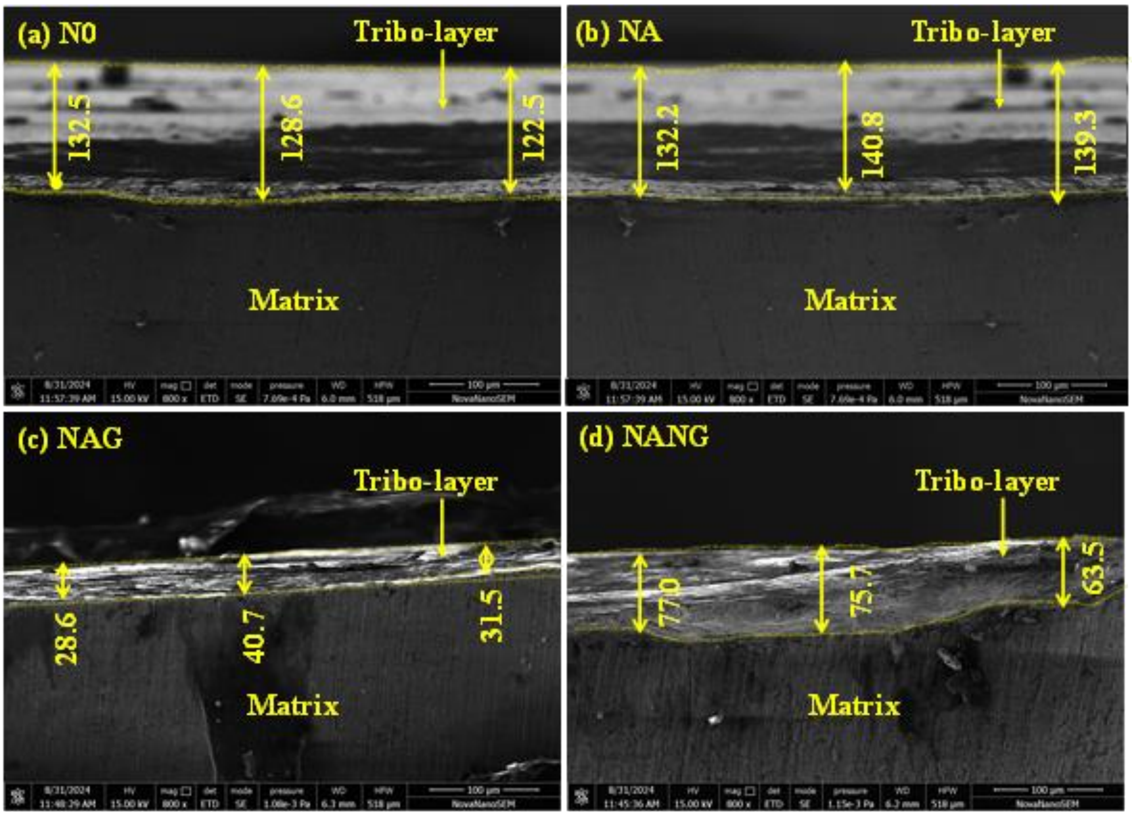

Fig. 4. 24 Cross-sectional FESEM micrographs of the worn subsurface at 800 °C corresponding to (a) N0, (b) NA, (c) NAG, and (d) NANG

The observed fluctuations in the coefficient of friction (CoF) for N0 and the composites, as seen in Fig. 4.11, may be explained based on the initial surface roughness of the mating bodies. At the beginning of the sliding motion between the tribo-pair, the contact occurs at some discrete asperities. These asperities get evened out as the sliding progresses, and eventually, the surfaces attain better conformity with each other, resulting in a stabilization of CoF [39]. While initial roughness influences early fluctuations, the prolonged variations in CoF may be due to material transfer, third-body effects, wear debris accumulation, and thermal influences. These factors cause intermittent changes in surface interactions, preventing complete stabilization.

The friction and wear behaviour of base alloy and composites may be elucidated on the basis of their hardness and the worn surface features like ploughing marks (deep/shallow or wide/fine), loose wear particles, nature of the transfer layer of wear debris (loosely bound/well-compacted or continuous/scattered), the area coverage of transfer layer (complete/partial) and lubricious species contained in the transfer layer. It is an established fact that the harder the material, the better its resistance to wear [28]. The existence of loose wear particles causes abrasion, resulting in a larger loss of material. A loosely bound and scattered transfer layer with partial area coverage enables the direct interaction between the mating pair during sliding, leading to an increase in both the friction and the wear. However, a well-compacted and continuous transfer layer covering a larger area of surface restricts the direct contact between the tribo-pairs, resulting in a decrease in friction and wear. The presence of lubricious species offers low shearing junctions at the interface, which help in the reduction of friction. The occurrence of a synergistic action between the solid lubricants also affects tribological behaviour. However, the final performance depends on the relative domination of the various tribo-chemical processes taking place during sliding.

A relatively higher average CoF of N0 at RT in comparison to 200, 400, 600, and 800 ^{o}C as seen from Fig. 4.12, may be attributed to the presence of loose wear particles over the worn surfaces of N0 (Fig. 4.14 (a)) and the ball slid against it (Fig. 4.15 (a)) at RT. However, a significant decrease in CoF from RT to 200 ^{o}C and a gradual decrease in-between 400 and 600 ^{o}C may be ascribed to the presence of a relatively compact transfer layer containing oxides of the constituent elements of N0, namely, NiO, MoO_3, $NiMoO_4$, and $NiCr_2O_4$ at 200, 400, and 600 ^{o}C (Figs. 4.14 (c, e, and g)) on the worn surface of N0 as evident from the XRD and Raman spectra of N0 shown in Fig. 4.22 (a) and Fig. 4.23(a), respectively, and the presence of compacted layer of wear debris on the counterface balls (Figs. 4.15 (c, e, and g)). The oxides such as NiO, MoO_3, NiMoO4, and $NiCr_2O_4$ have been reported to be lubricious in nature by several authors [67,94] and provide low shearing capability at the interface. However, an increase in specific wear rate from RT to 600 °C despite a decrease in CoF may be due to the presence of loose wear particles, ploughing marks, or a discontinuous transfer layer on the worn surfaces of the N0 (Figs. 4.14 (a, c, e, and g)) and the corresponding counterface (Figs. 4.15 (a, c, e, and g)) which might have given rise to direct contact between mating bodies and hence, a relatively larger loss of material. A sharp decrease in both the average CoF and the specific wear rate beyond 600 °C (Figs. 4.12 and 4.13) may be explained based on the presence of a smooth and well-compacted transfer layer containing lubricious oxides covering almost the entire area of the worn surface of N0 (Fig. 4.14 (i)) and the counterface ball (Fig. 4.15 (i)). The larger area coverage provided by the transfer layer diminishes the possibility of direct contact between the mating materials transfer layer, whereas the presence of lubricous species endows the surface with low shearing capability, which help in reducing both the CoF and wear rate. The presence of oxides has been confirmed by XRD (Fig. 4.22 (a)) and Raman spectra (Fig. 4.23 (a)) of the worn surface of N0. EDS analysis of the worn surface of the base alloy EDS (Figs. 4.14 (b, d, f, h, and j)) and counter ball (Figs. 4.15 (b, d, f, h, and j)) has confirmed the presence of oxygen and transfer of material from N0 to the ball.

A relatively higher CoF for NA at RT compared to 200, 400, 600, and 800 °C (Fig. 4.12), can be explained based on the presence of wear debris on the worn surface of tribo-pairs as shown in Figs. 4.16 and 4.17. A significant reduction in the CoF from RT to 200 °C for NA may be ascribed to the presence of Ag, which smears on the worn surface and provides easy-to-shear junctions at the contact interface[39]. The average CoF remains almost constant from 200 to 400 °C, which may be credited to the presence of a transfer layer on the surface of tribo-pairs worn at 200 and 400 °C as shown in Figs. 4.16 (c and e) and Figs. 4.17 (c and e). A decrease in CoF from 400 to 600 °C might be due to the existence of a smooth transfer layer on the worn surface of NA (Fig. 4.16 (g)) and counter ball (Fig 4.17 (g)) at 600 ºC. The transfer layer consisting of lubricious species such as elemental Ag, NiO, $NiMoO_4$, MoO_3, Ag_2MoO_4, and $Ag_2Mo_2O_7$ has been confirmed by XRD (Fig. 4.22 (b)) and Raman spectra (Fig. 4.23 (b)). A further decrease in CoF from 600 to 800 ºC may be ascribed to the presence of a well-compacted tribo-layer on the worn surface of NA (Fig. 4.16 (i)) and counter ball (Fig. 4.17 (i)) at 800 ºC. The transfer layer on the worn surface of NA consists of lubricious species at 600 ºC as verified by XRD and Raman spectra shown in Fig. 4.22 (b) and Fig. 4.23(b), respectively. The lubricious nature of silver molybdates has also been reported by other researchers [37,95]. The increase in the specific wear rate of NA from RT to 400 ºC may be explained based on the features present on the worn surfaces of NA and the corresponding ball. The presence of fine sliding marks and a layer of Ag covering the entire worn surface of NA and counter ball (Figs. 4.16 (a) and 4.17 (a)) at RT might have inhibited the direct contact between the tribo-pair, leading to a relatively smaller loss of material. One may observe the presence of wider sliding marks on the worn surface of NA at 200 and 400 ºC apart from a transfer layer with different area coverage and delamination at a few places, as seen from Figs. 4.16 (c and e) and the presence of a discontinuous layer of transferred material at the counterface ball (Figs. 4.17 (c and e)). All these factors may have raised the possibility of direct contact between mating materials and increased the volume loss, as seen in Fig. 4.13. However, a decrease in specific wear rate beyond 400 ºC may be explained by the presence of a compact and continuous transfer layer containing lubricious oxides of Ni and Mo apart from silver molybdates on the contact surface of NA and the counter Si_3N_4 ball at 600 and 800 ºC as shown in Figs 4.16 (g and i) and Fig. 4.17 (g and i), which restricts the direct contact between the mating bodies. The presence of a transfer layer having lubricious species assists in lowering both the coefficient of friction and specific wear rate by endowing the surface with easy-to-shear capability. EDS analyses of the NA and counter ball at RT, 200, 400, 600, and 800 °C reveals the presence of oxygen as shown in Figs. 4.16 (b, d, f, h, and j) and Figs. 4.17 (b, d, f, h, and j), validating the results of XRD and Raman spectra as seen from Figs 4.22 (b) and 4.23 (b). A lower specific wear rate observed for NA as compared to N0 from RT to 400 °C may be attributed to the lubrication provided by the silver despite a relatively low hardness of NA. However, a tribo-layer containing silver molybdates and oxides of Ni and Mo might have been the governing factor in reducing material loss for NA as compared to N0 at 600 and 800 °C. The relatively higher thickness of the transfer layer on the worn surface of NA compared to N0 at 800 °C as evidenced by Figs. 4.24 (a and b) might also have contributed in lowering down the CoF and wear rate for NA.

A decrease in the average CoF for NAG (Fig. 4.12) from RT to 200 °C may be credited to the presence of rGO and silver over the worn surfaces of NAG (Figs. 4.18 (a and c)) and counter ball (Figs. 4.19 (a and c)). However, an almost stable CoF from 200 to 600 °C may be attributed to the presence of a transfer layer consisting of rGO, Ag, oxides of Ni and Mo, and silver molybdates present over the worn surfaces of NAG (Figs. 4.18 (c, e, and g)) and the ball slid against NAG (Figs. 4.19 (c, e, and g)) as confirmed by EDS (Figs. 4.18 (d, f, and h) and 4.19 (d, f, and h)), XRD (Fig. 4.22 (c)), and Raman spectra (Fig. 4.23 (c)). A slight increase in CoF from 600 to 800 °C could be due to the loss of lubricating efficacy of rGO at this temperature, as reported earlier also by Xiao et al. [96]. The delamination of the tribo-layer as seen in Fig. 4.18 (c) might have caused an increase in the specific wear rate for NAG (Fig. 4.13) from RT to 200 °C. The increased possibility of direct contact between tribo-pair at 200 °C might also have contributed to the increased material loss as judged by the presence of scattered layers of transferred material on the worn surface of the ball (Fig. 4.19 (c)). The specific wear rate does not show any discernible variation from 200 to 600 °C, probably due to the existence of the transfer layer and similar area coverage and degree of compaction over the worn surfaces of tribo-pair as seen from a comparison of Figs. 4.18 (c, e, and g) and Figs. 4.19 (c, e, and g). However, the presence of a well-compacted tribo-layer containing lubricating species on the worn surface of NAG (Fig. 4.18 (i)) and its counter ball (Fig. 4.19 (i)) might have reduced specific wear rate beyond 600 ^{o}C by hindering the direct interaction between the composite and counterpart ball.

A relatively lower average CoF for NAG from RT to 600 ^{o}C compared to NA (Fig. 4.12) may be due to assistive action between Ag and rGO in providing effective lubrication in this range. However, a higher CoF observed for NAG than NA at 800 ^{o}C suggests the loss of synergetic action between rGO and silver. It is believed that rGO may have suppressed the formation of silver molybdate, as evidenced by the non-existence of Ag_2MoO_4 in the XRD pattern of NAG at 800 ^{o}C. Ibrahim et al. [97] also found that by incorporating 10 wt.% silver and 1.5 wt.% GNPs in the NiAl matrix exhibit low CoF compared to NiAl +10 wt.% silver at RT when sliding against Si_3N_4. The increased specific wear rate for NAG in comparison to NA at temperatures except at 400 ^{o}C may be explained based on the presence of the different features on the worn surfaces of composite and ball, such as sliding marks (fine or wide), transfer layer (scattered or continuous), its area coverage over the substrate and degree of compaction (loosely bound or compact) which govern the possibility of direct interaction between the hard asperities of the counterface ball and the composite and in turn increased specific wear rate. A visualization and comparison of SEM images of Figs. 4.16, 4.17, 4.18, and 4.19, indicate a higher possibility of direct interaction between the mating material for NAG than NA, which may account for a larger specific wear rate in NAG, as explained earlier. The smaller thickness of the transfer layer on the worn surface of NAG at 800^{o}C compared to N0 and NA as seen from Figs. 4.24 (a-c) might have allowed the penetration of this layer by the asperities of counterface leading to a higher CoF for NAG than N0 and NA. However, a relatively higher hardness of NAG compared to NA might have played a dominating role in controlling the material loss rather than the presence of a transfer layer leading to a lower wear rate.

A sharp decrease in CoF of NANG from RT to 200 ºC, as seen in Fig. 4.12, may again be explained on the basis of low shearing junctions at the contact interface due smearing of Ag and the presence rGO on the surface. Almost constant average CoF of NANG from 200 to 600 ºC may be credited to the existence of rGO-Ni, silver, and the lubricious oxides of Ni and Mo, in addition to silver molybdates, over the worn surfaces of NANG (Figs. 4.20 (c, e, and g)), depending upon the temperature, and the worn surface of the ball slid against NANG (Figs. 4.21 (c, e, and d)), as substantiated by XRD (Fig. 4.22 (d)) and Raman spectra (Fig. 4.23 (d)). The slight increase in CoF from 600 to 800 ºC could be due to the diminished lubricating capability of rGO-Ni at this temperature. A slight increase in the specific wear rate of NANG from RT to 200 ºC, as seen in Fig. 4.13, may be due to the increased possibility of direct contact between the composite and counterface ball as indicated by the presence of a discontinuous transfer layer over the worn surface of NANG at 200 ºC and wider ploughing marks in comparison to those seen at RT (Figs. 4.20 (a and c)) and presence of loose wear debris on the counter ball (Figs. 4.21 (a and c)). A decrease in specific wear rate from 200 to 600 ºC may be attributed to the presence of a continuous and well-compacted tribo-layer over the worn surface of NANG (Figs. 4.20 (c, e, and g)) as well as on the counterface ball (Figs. 4.21 (c, e, and g)), which might have restricted the direct contact between the ball and the composite. The increase in specific wear rate for NANG at 800 ºC may be due to the presence of a discontinuous tribo-layer covering a relatively lesser area of the surface over the worn surface of NANG (Fig. 4.20 (i)), which might have given rise to a relatively larger loss of materials due to inadequate inhibition of direct contact between the ball and the composite as stated earlier also. The delamination of the transfer layer at a few locations on the worn surface of the ball as seen from Fig. 4.21 (i) might also have resulted in the increased contact. A higher thickness of the transfer layer on the worn surface of NANG compared to NAG at 800 ºC, as illustrated in Figs. 4.24 (c and d) may have been responsible for a lower CoF as well as wear rate for NANG than NAG.

Based on the morphology of the worn surface, the dominant wear mechanisms for N0 and NA have been found to be ploughing and delamination from RT to 400 ºC, which changes to oxidative wear at 600 and 800 ºC. However, the wear mechanisms for NAG and NANG are ploughing and delamination from RT to 200ºC, delamination at 400ºC and a combination of abrasion and oxidation at 600 and 800ºC as revealed by the worn surface morphologies at these temperatures.

The lowest CoF and wear rate shown by NANG from RT to 600 ºC reflects the manifestation of synergistic lubrication between Ag and rGO-Ni apart from the improved integration of rGO-Ni in the matrix. This shows that a combination of Ag and rGO-Ni reduces both the CoF and the specific wear rate from RT to 600 ºC by supporting each other's lubricating capabilities. An increased CoF at 800 ºC for NAG and NANG could be due to the possible loss of assistive action between Ag and rGO/rGO-Ni.

To summarize, the composite NANG containing 10 wt.% Ag and 1wt.% rGO-Ni, i.e., NANG has shown the lowest CoF and wear rate among all the materials at temperatures from RT to 600 ºC, which reflects the cooperative synergy between Ag and rGO in attaining low friction and wear over this range of temperature. The wear rate shown by NANG is almost same as that of NA at 800 ºC despite the presence of rGO which indicates the probable loss of assistive action between Ag and rGO at this temperature.